

# Volcanism, mineralization and metamorphism at the Xitieshan Pb–Zn deposit, NW China: Insights from zircon geochronology and geochemistry

Huashan Sun <sup>a</sup>, Huan Li <sup>a,\*</sup>, Noreen J. Evans <sup>b</sup>, Hui Yang <sup>a</sup>, Pan Wu <sup>a</sup>

<sup>a</sup> Faculty of Earth Resources, China University of Geosciences, Wuhan 430074, China

<sup>b</sup> John de Laeter Centre, TIGER, Applied Geology, Curtin University, Bentley 6845, Australia



## ARTICLE INFO

### Article history:

Received 6 February 2017

Received in revised form 26 April 2017

Accepted 7 May 2017

Available online 17 May 2017

### Keywords:

Zircon geochemistry

Metamorphic fluid

VSHMS

Xitieshan

Tanjianshan, North Qadair

## ABSTRACT

The footwall volcanic rocks of the Ordovician Tanjianshan Group in the world-class Xitieshan Pb–Zn deposit have experienced prolonged arc volcanism followed by strong metamorphism and deformation. This has resulted in a complex thermal history and led to ambiguity in interpretation of zircon geochronological results. An integrated study involving textural characterization, CL imaging, trace element analysis, Ti-in-zircon thermometry and LA-ICPMS U–Pb dating has provided tight constraints on the age and genesis of the zircon groups in the volcanic rocks. The temperature of metamorphism and deformation indicated by metacryst minerals and micro-structures in the volcanic rocks ranges from 550 to 650 °C, which partially overlaps with the lower temperature range of zircon crystallization (600–750 °C) calculated using the Ti-in-zircon thermometer. Cathodoluminescence images and trace element compositions confirm a magmatic origin for the zircons, which have also been variably altered by metamorphic fluids. Two ranges of U–Pb ages, 475–470 Ma and 460–450 Ma, have been obtained on typical magmatic zircons and are interpreted to represent pre-mineralization arc volcanism in the Xitieshan deposit. A younger age group of 440–430 Ma for the fluid-modified zircons is considered to record post-ore metamorphism during the North Qadair Orogeny. Thus, we propose that the original exhalative ores at the Xitieshan Pb–Zn deposit formed at 450–440 Ma.

© 2017 Elsevier B.V. All rights reserved.

## 1. Introduction

Zircon U–Pb dating of volcanic rocks can constrain the timing of mineralization at ancient submarine massive sulfide deposits (e.g., Page and Laing, 1992; Barrie et al., 2002; Piercy et al., 2008; Rosa et al., 2009; Fu et al., 2017). Prolonged volcanism (pre-, syn- and post-mineralization) and post-mineralization metamorphism make interpretation of zircon U–Pb age data complicated (e.g., Barrie et al., 2002; Rosa et al., 2009). However, accurately deciphering the chronology is the key to comprehensively understanding the genesis of ancient submarine massive sulfide deposits. The world-class Xitieshan Pb–Zn deposit, located in the Caledonian orogenic belt and hosted within volcanic and sedimentary rocks, provides an excellent natural laboratory in which to deconvolve these complex geochronological events through comprehensive characterization and analysis.

The Xitieshan volcanic and sediment-hosted Pb–Zn deposit, located at the northern margin of Qaidam Basin (NMQB, Fig. 1), NW China, has been the focus of prospecting and mining activity since the 1980s. As of 2014, the total ore reserves were estimated to be >60 Mt, with Pb + Zn metal reserves of >6 Mt and average Pb + Zn grade of ~9% (Fu et al., 2017). Moreover, there are considerable prospective reserves of Au, Ag and S (Hou et al., 1999). The Pb–Zn ore bodies are hosted in the lower section of Ordovician Tanjianshan Group, which comprises two volcanic-sedimentary cycles. Previous petrological and geochemical studies have documented that the volcanic rocks in the lower section of the Tanjianshan Group are bimodal in composition, whereas those in the upper section are intermediate-basaltic (Wu et al., 1987; Sun et al., 2012; Fu, 2015). Up until the 1990s, the tectonic setting was thought to be a continental margin rift (Wu et al., 1987; Xiong and Chen, 1994). However, the discovery of an eclogite-bearing ultra-high-pressure (UHP) metamorphic belt in the NMQB (Yang et al., 2001) led to the recognition of early Paleozoic ocean-continent subduction and orogenic events (Song et al., 2004, 2009; Zhang et al., 2009b, 2013; Xiong et al., 2014). An island arc tectonic

\* Corresponding author.

E-mail address: [lihuan@cug.edu.cn](mailto:lihuan@cug.edu.cn) (H. Li).

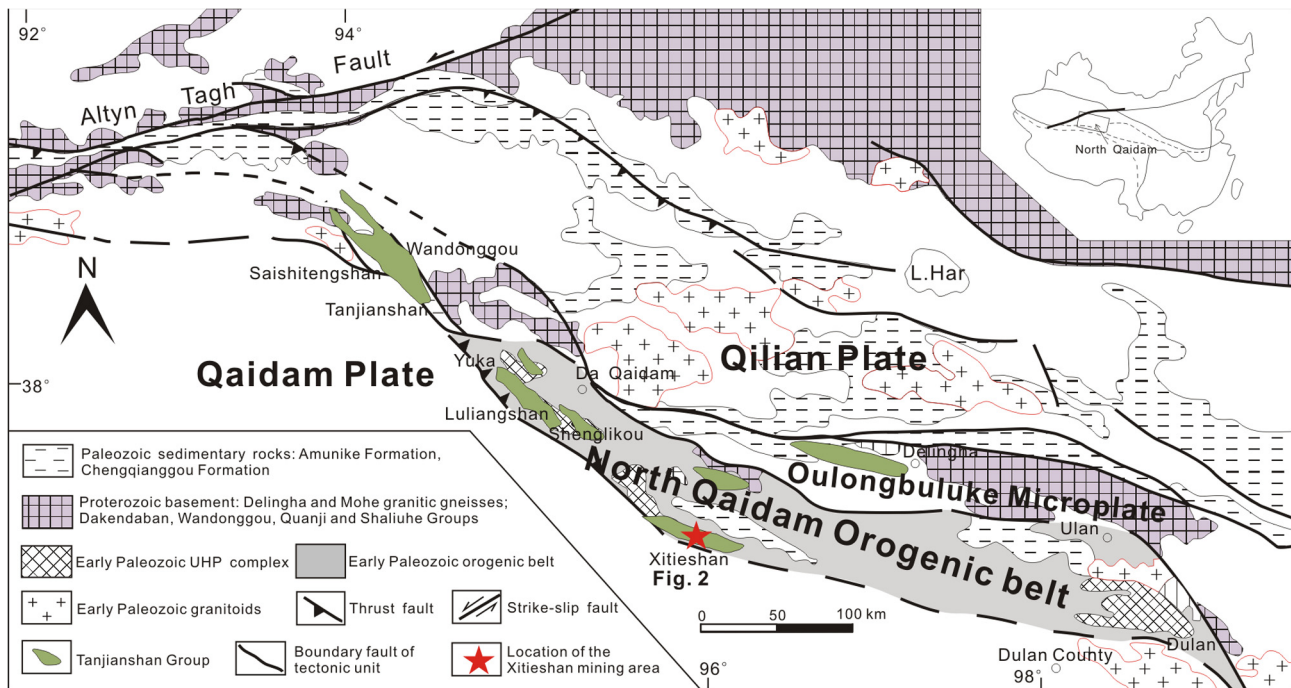


**Fig. 1.** Geological map of the northern margin of Qaidam basin, showing major tectonic units, distribution of the Tanjianshan Group and location of the Xitieshan deposit (after Xin et al., 2006).

setting has also been recently proposed (Wang et al., 2004; Shi et al., 2006; Xiong et al., 2014; Li and Xi, 2015).

The timing of mineralization at the Xitieshan Pb-Zn deposit has not been definitively established. Based on the fossil record in sedimentary rocks in the lower section of the Tanjianshan Group (*Ambalodus cf. triangularis* Bransan and Mehl), Wu et al. (1987) suggested that the mineralization was Upper Ordovician. Zhao et al. (2003) determined a zircon U-Pb age of  $486 \pm 13$  Ma for the felsic volcanic units in the group close to the footwall of ore-body, suggesting that the mineralization occurred in the Lower Ordovician. Recently Liang et al. (2014) used laser ablation-inductively coupled plasma mass spectrometry (LA-ICPMS) to acquire a zircon U-Pb age group of 458–463 Ma for the felsic volcanic rocks, and Fu (2015) and Fu et al. (2017) reported zircon U-Pb ages of 461–452 Ma for the same felsic volcanic rocks in the deposit. Based on metamorphic mineral assemblages and microstructural deformation analyses of the Tanjianshan Group, coupled with zircon cathodoluminescence (CL)-imaging, geochemistry, Ti-in-zircon thermometry and LA-ICPMS zircon U-Pb dating, this study systematically dissects the implications of new zircon U-Pb ages determined on felsic volcanic rocks, and aims to offer insights into the epochs of original exhalative ore-formation and post-ore modification in the Xitieshan deposit.

## 2. Regional geology

The NMQB is a compound collision orogenic belt, 700 km in length and 30–60 km wide, resulting from amalgamation of the Qilan and Qadaim Plates during the Rodinia and Caledonian periods (Lu et al., 2002; Xu et al., 2003; Song et al., 2004, 2009). The NMQB is composed of three tectonic units: the Oulongbuluke microplate to the north, Qadaim Plate to the south and the NMQB compound collision orogenic belt in between (Fig. 1). The Oulongbuluke microplate, located in the south of the Qilan Plate, is the oldest micro-continent in the region, with a typical double-layered Paleo-Mesoproterozoic architecture in the basement and

Nanhua-Sinian strata making up the cover. The Paleo-Mesoproterozoic basement is composed of a metamorphic complex including the Delingha gneiss (zircon U-Pb  $2412 \pm 14$  Ma,  $2366 \pm 10$  Ma; Lu et al., 2002), Mohe granitic gneiss (zircon U-Pb  $2479 \pm 19/18$  Ma; Li et al., 2007), Dakendaban Group (zircon U-Pb  $1939 \pm 21$  Ma; Hao et al., 2004b) and the Mesoproterozoic Wandonggou Group. The Nanhua-Sinian strata formed in a well-documented period corresponding to continental break-up in the Late Neoproterozoic (zircon U-Pb  $739 \pm 28$  Ma; Li et al., 2003), referred to as the Quanji Group. The NMQB compound collision orogenic belt experienced two amalgamations including the Meso to Neo-proterozoic Rodinia Supercontinent and Early Paleozoic collision between the Oulongbuluke and the Qadaim Plates. The former is represented by arc-setting granitic gneiss, making up the dominant component of the Shaliuhe Group (zircon U-Pb  $1020 \pm 41$  Ma,  $987 \pm 93$  Ma,  $952 \pm 13$  Ma, Hao et al., 2004a). The latter is manifested by the arc volcanism of Tanjianshan Group along the NMQB (Fig. 1, LA-ICPMS zircon U-Pb  $496.3 \pm 6.2$  Ma, Yuan et al., 2002;  $486 \pm 13$  Ma, Zhao et al., 2003;  $514.2 \pm 8.5$  Ma, Shi et al., 2006;  $460\text{--}445$  Ma, Liang et al., 2014) and the eclogite within the Shaliuhe Group. The basement of the Qadaim plate is not well understood due to extensive Quaternary cover. Early Paleozoic granitoids related to subduction and collision processes occur extensively with ages ranging from ca. 470 Ma to 390 Ma (Fig. 1, Wu et al., 2004, 2007). Xiong et al. (2014) further distinguished two orogenic stages in the Early Paleozoic: ocean (South Qilian Ocean)–continent (Qilan Plate) subduction (540–460 Ma) and subsequent collision and exhumation (460–420 Ma). Afterwards, erosion dominated this area and resulted in the polymictic conglomerate and sandstone sediment of the Late Devonian to Early Carboniferous, named the Amunike Formation. Sediments were intensively deposited along the rift basins at the northern and southern margins of the Qaidam Basin, continuous with the early Carboniferous Chengqianggou Formation which is composed of littoral facies limestone and sandstone. In the Late Carboniferous, the taphrogenic trough in the NMQB initiated strong intracontinental inversion-folding and uplifting, whereas

the ocean-continent transformation in the southern margin of Qaidam Basin was delayed until the Late Permian to Middle Triassic (Xin et al., 2006; Zhang et al., 2009a). During the Mesozoic and Cenozoic, the NMQB experienced terrestrial basin formation and subsequent plateau uplift, triggered by the Himalayan Orogeny (Xin et al., 2006).

### 3. Deposit geology

#### 3.1. Stratigraphic features

The outcropping strata from north to south in the Xitieshan mining area include the Shaliuhe Group, Ordovician Tanjianshan Group, Devonian Amunik Formation and Carboniferous Chengqianggou Formation (Fig. 2). The Shaliuhe Group is a dominant component of the UHP metamorphic belt. The Ordovician Tanjianshan Group was further divided into four formations based on lithological association, namely A, B, C and D. Formation A can be further subdivided into two sub-members, A-1 and A-2. The former is characterized by bimodal volcanics and the latter is dominated by sedimentary/metamorphic rocks including carbonaceous muscovite-quartz schist, marble, chlorite-quartz schist and sedimentary exhalative rocks, e.g., ferro-manganese carbonate and quartz albitite (Deng et al., 2003; Zhu et al., 2007). Formation B comprises intermediate-basaltic volcanics while Formation C consists of purple-reddish polymictic conglomerate, pebbly sandstone, sandstone and siltstone, in which greenschist pebbles (related to the process of orogeny) are also present. Based on these greenschist pebbles, Li et al. (2006) proposed taking Formation C out of the Tanjianshan group and redesignating it as a sedimentary sequence in a post-collisional foreland basin. Formation D is composed of a series of basaltic volcanics interbedded with sedi-

mentary rocks. Geochemically, Formation A-1 and B are calcalkaline in composition, enriched in light rare earth elements (LREEs) and large ion lithophile elements (LILEs; e.g., K, Rb, Ba, Th, Ce, Sm), depleted in high field strength elements (HFSEs; e.g., Nb, Ta, P, Ti), characterized by a slightly negative Eu anomaly, high and large variable  $\epsilon\text{Sr}(t)$  (35.8–207.3) and low or close to mantle  $\epsilon\text{Nd}(t)$  (−12.6 to 0.5). In contrast, Formation D is tholeiitic, showing weak enrichment of LREEs and LILEs (e.g., K, Rb, Ba), characterized by flat REE and E-MORB-like patterns, with no Eu anomalies. It has a relatively low  $\epsilon\text{Sr}(t)$  (8.0–41.5) and high  $\epsilon\text{Nd}(t)$  (−2.8 to 7.0) (Sun et al., 2012).

#### 3.2. Metamorphic characteristics

Metamorphism occurred intensively within the Tanjianshan Group. The common metacrust assemblage includes epidote, actinolite, zoisite, chlorite, albite, plagioclase and hornblende in the intermediate-basaltic volcanic rocks but is dominated by muscovite, quartz and minor chlorite in the sedimentary rocks. Ductile deformation is very common within the Tanjianshan Group, showing up in outcrop as recumbent folds, dissymmetric Z-shaped folds, parasitic folds formed by metamorphic separated quartz veins, rootless intrafolial folds composed of thin-bedded marble or siliceous rocks, mullions and boudinage. Additionally, mylonitic fabric is observed extensively under the microscope and ductile deformation is superimposed on brittle deformation, as seen in a series of thrust faults and shear fractures (Fig. 2). The phenomena of two-phase deformation, (i.e., the early ductile deformation over rotation or orientation of metacrysts and the late brittle deformation cross-cutting the former as microfractures), can also be observed under the microscope (Fig. 3a).

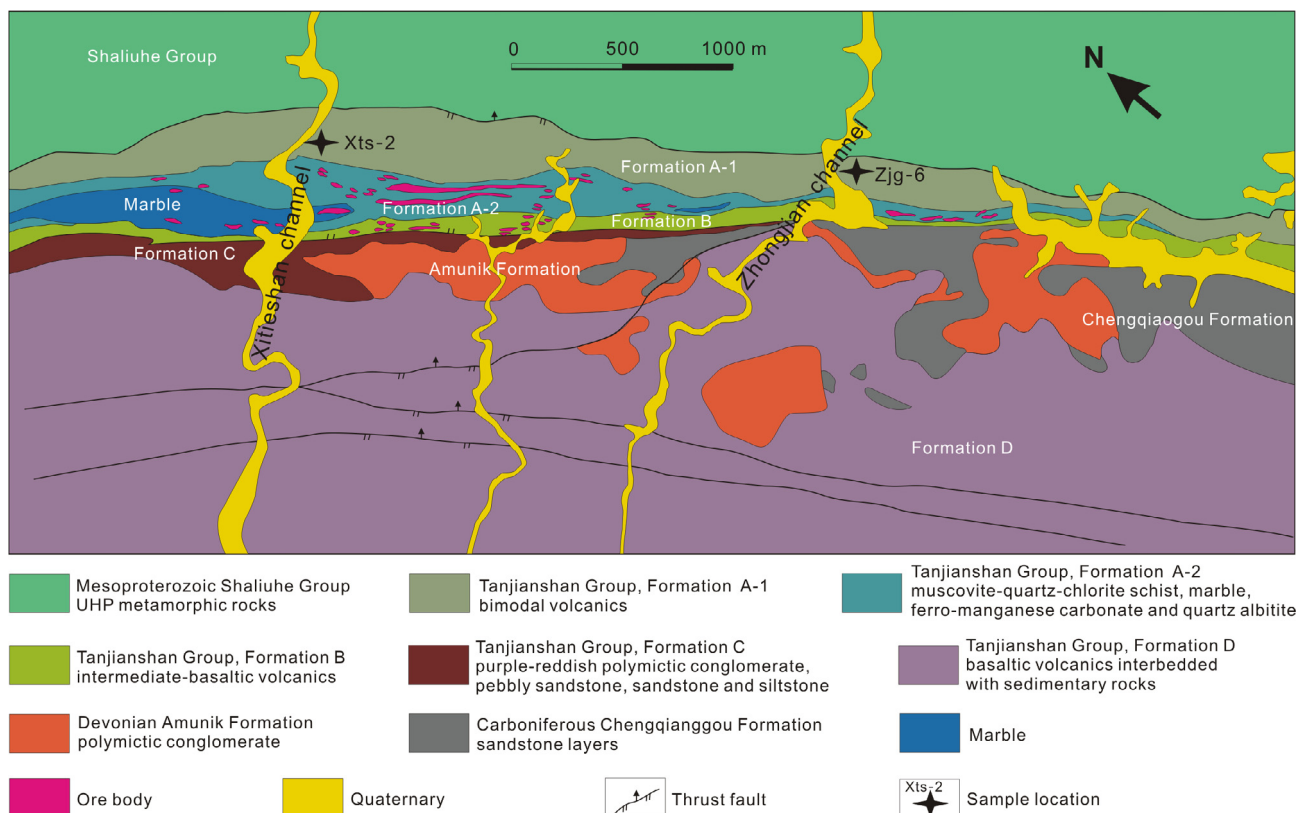
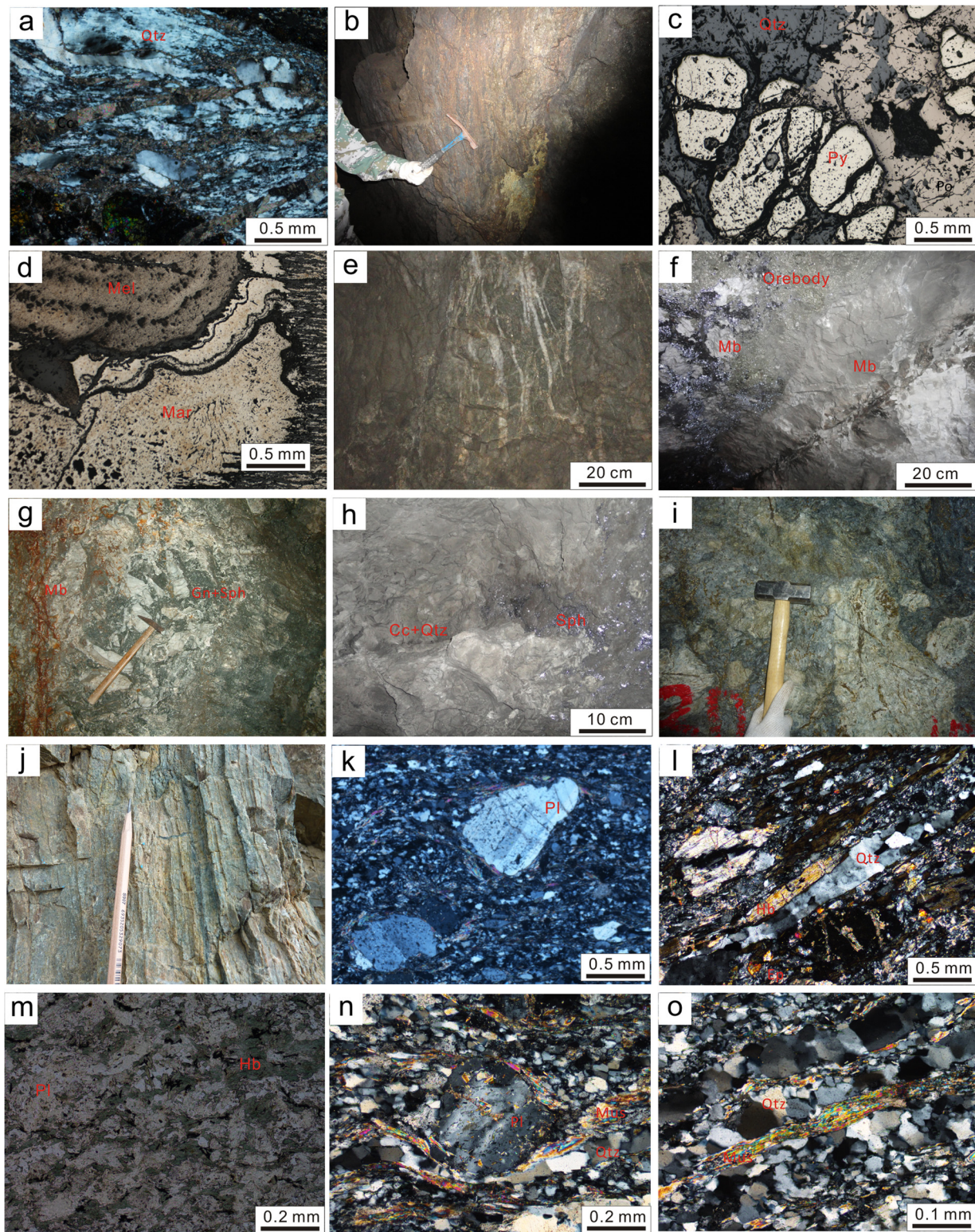


Fig. 2. Geological map of the Xitieshan deposit (after Sun et al., 2012).



**Fig. 3.** Field and microscope photos showing mineralogy and microstructural deformation for ore bodies and host rocks. (a) Two-stage deformation, early ductile and late brittle in cross-polarized light; (b) conformable ore body hosted in schist, yellowish minerals (mainly pyrites) are more abundant than blackish minerals (galena and sphalerite); (c) dominant mineral assemblage of Py + Po + Qtz for the conformable ore body; (d) melnikovite and marcasite in the yellowish minerals (mainly pyrites); (e) undeformed veinlets of quartz and pyrite indicate post-mineralization reworking; (f) undeformed ore body filled in the brittle fractures within marble, the contact zone between ore body and marble is bleached; (g) undeformed angular marble-breccias cemented by blackish sulfide minerals; (h) numerous vugs filled by Cc + Qtz + Sph; (i) variable size of schist-breccias proximal to the orebody with decolorization, silicification, sericitization and pyrite veinlets, likely represent the proxy of exhalative conduit; (j) alternative band of andesite and dacite where sample XTS-2 was taken; (k) porphyritic texture, plagioclase porphyroblast with a sinistral rotation in sample XTS-2, cross-polarized light; (l) metacrystal mineral assemblage of Hb + Ep + Pl + Qt in sample XTS-2, cross-polarized light; (m) metacrystal mineral assemblage of Hb (chloritized) + Pl + Qt in sample ZJG-6, plane-polarized light; (n) multi-quartz ribbons without significant strain, with the long axis of a feldspar porphyroblast perpendicular to the foliation in sample XTS-2, cross-polarized light; (o) multi-quartz ribbons without significant strain in sample ZJG-6, cross-polarized light. Py: pyrite, Po: pyrrhotite, Mel: melnikovite, Mar: marcasite, Gn: galena, Sph: sphalerite, Hb: hornblende, Pl: plagioclase, Ep: epidote, Qt: quartz, Mus: muscovite, Cc: calcite.

### 3.3. Mineralization

Hosted by both sedimentary and volcanic rocks, the Xitieshan deposit has features similar to both sedimentary exhalative (SEDEX) deposits and VMS deposits, and thus can be classified as a volcanic and sediment-hosted massive sulfide (VSHMS) deposit (Feng et al., 2010; Fu et al., 2017). Two types of mineralization can be recognized according to the relationship between ore bodies and wall rocks. One is conformable mineralization, mainly hosted by marble in the lower section of Formation A-2 and at the contact boundary between Formations A and B. This type of mineralization is characterized by pyrite, pyrrhotite, melnikovite and marcasite, without obvious wall-rock alteration (Fig. 3b-d). It is commonly superimposed by orogenic/post-orogenic undeformed quartz-pyrite veinlets (Fig. 3e). Another type of mineralization is unconformable and hosted dominantly within the thick-bedded marble of the upper section of Formation A-2 and secondarily within varieties of schist. It is apparently controlled by brittle fractures and can be further grouped into two subtypes from the perspective of deformation and wall-rock alteration. The first subtype is undeformed, hosted in the thick-bedded marble (Fig. 3f). It is characterized by angular marble-breccias cemented or replaced by a higher abundance of galena and sphalerite over pyrite (Fig. 3g) and numerous intact vugs filled by quartz, calcite and sphalerite (Fig. 3h). The second subtype is also controlled by brittle fractures; however, the deformation and alteration are apparently stronger. Deformed and schist-altered breccias were cemented by disseminate pyrite veinlets. The size of breccias varies widely, commonly with obtuse angled shapes. Intensive decolored alteration includes silicification, sericitization, kaolinization, carbonatization and veinlet-disseminate pyritization (Fig. 3i). The first subtype likely represents the latest period of mineralization post-orogeny, whereas the second subtype may be associated with original exhalative conduits.

### 4. Samples and analytical procedures

For LA-ICPMS zircon U-Pb dating and trace element analysis, two samples were taken from the Tanjianshan Group Formation A-1 (Fig. 2). Sample XTS-2 ( $37^{\circ}19'59.27''\text{N}$ ,  $95^{\circ}34'4.44''\text{E}$ ) was taken from the Xitieshan channel, ~10 m below the bottom of Formation

A-2. Sample ZJG-6 ( $37^{\circ}18'52.91''\text{N}$ ,  $95^{\circ}34'59.57''\text{E}$ ) was taken from the Zhongjian channel which is close to the Proterozoic Shaliuhe Group. Sample XTS-2 is composed of alternating bands of andesite and rhyodacite with bands varying from 1 to 5 cm in width (Fig. 3j). The sequence where XTS-2 lies is at least 20 m thick. Rhyolitic dacite occurs as light colored bands with blastoporphyritic texture seen under the microscope. The phenocrysts are plagioclase porphyrocrysts with a sinistral rotation (Fig. 3k), whereas the matrix is granolepidoblastic in texture, composed of metacrysts of quartz, plagioclase, muscovite and epidote. Andesite occurs as grey greenish bands with fine-granular and columnar mosaic texture, composed of hornblende (partial chloritization), plagioclase, epidote and quartz (Fig. 3l). Sample ZJG-6 represents a ~8 m thick dacite sequence. It is characterized by an equigranular metacrystal texture with minor plagioclase porphyroclasts, dominantly composed of hornblende (with partial chloritization), plagioclase and quartz (Fig. 3m). The metacrystal mineral assemblages from the two samples indicate the metamorphic grade was epidote-amphibolite to amphibolite. In addition, it is worth pointing out that quartz ribbons (with an absence of significant strain, as also seen in high temperature mylonitization of quartzofeldspathic gneisses from the Schirmacher Hills, East Antarctica; Bose and Sengupta, 2003), are abundant in both samples (Fig. 3n, o).

Cathodoluminescence images were taken for all zircons at the State Key Laboratory of Geological Processes and Mineral Resources (GPMR), China University of Geosciences (Wuhan), using a scanning electron microscope equipped with an energy dispersive spectroscopy system and a CL3+ detector, operated at 15 kV and 20 nA. U-Pb dating and trace element analyses were conducted by LA-ICPMS at GPMR. Laser sampling was performed using a GeoLas 2005 excimer laser ablation system. An Agilent 7500a ICPMS instrument was used to acquire ion-signal intensities. Laser energy and frequency were 70 mJ and 8 Hz, respectively, with spot size of 32  $\mu\text{m}$  and ablated depth of 20–40  $\mu\text{m}$ . Helium was used as the carrier gas. Argon was used as the make-up gas and mixed with the carrier gas via a T-connector before entering the ICP. Nitrogen was added into the central gas flow (Ar + He) of the Ar plasma to decrease the detection limit and improve precision (Hu et al., 2008). Each analysis incorporated a background acquisition of approximately 20–30 s (gas blank) followed by 50 s data acquisition from the sample. Detailed analytical conditions and

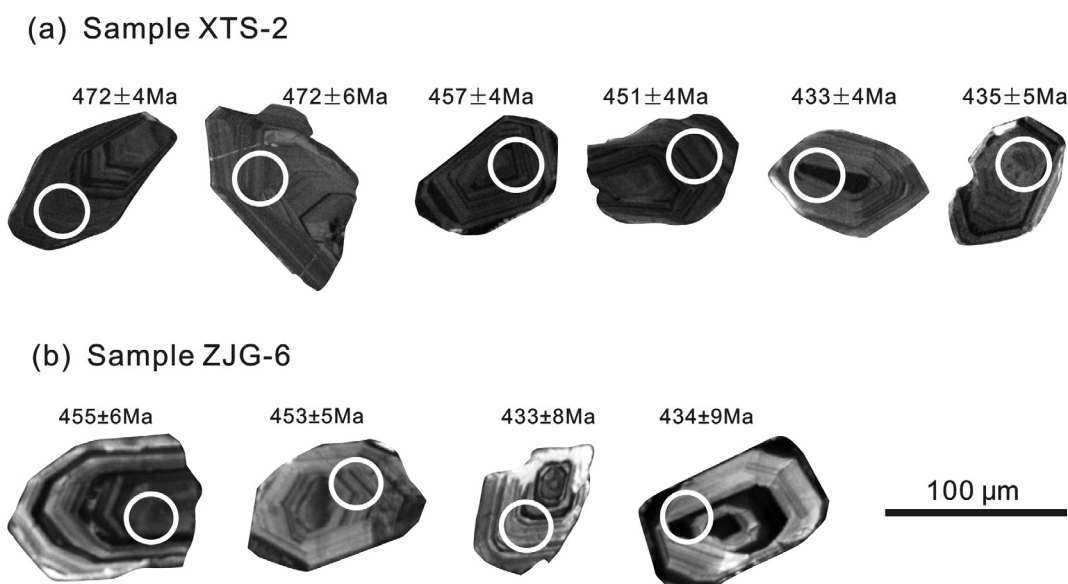


**Fig. 4.** CL-images of selected zircons for the samples XTS-2 (a) and ZJG-6 (b). White circles are locations of LA-ICPMS ablation.

procedures for zircon U–Pb dating are given in Liu et al. (2010a,b), and for trace elements analyses in Liu et al. (2008) and Chen et al. (2011). Zircon 91500 was used as the external standard for U–Pb dating, and was analyzed twice every five samples. Time-dependent drifts of U–Th–Pb isotopic ratios were corrected using a linear interpolation (with time) for every five analyses according to the variations of 91500. Preferred average U–Th–Pb isotopic ratios used for 91500 were calculated from Wiedenbeck et al. (1995) with uncertainties in preferred values propagated to the results for the unknowns (Liu et al., 2010b). In addition, GJ-1 (Jackson et al., 2004) was treated as a secondary standard, analyzed as an unknown. The weighted mean  $^{206}\text{Pb}/^{238}\text{U}$  age for GJ-1 was  $596.73 \pm 5.34$  Ma ( $2\sigma$ ,  $n = 25$ ), consistent within uncertainty with the recommended values (GJ-1:  $599.81 \pm 1.7$  Ma ( $2\sigma$ ), Jackson et al., 2004).

USGS reference glasses BCR-2G and BIR-1G were analyzed as external standards for trace element content calibration (Liu et al., 2008) with NIST 610 used to correct the time-dependent drift of sensitivity and mass discrimination (analyzed after every 10 unknowns). Trace element compositions of zircons were calibrated against multiple-reference materials (BCR-2G and BIR-1G), combined with internal standardization (Liu et al., 2010a). Off-line selection and integration of background and analytical signals, time-drift correction, and quantitative calibration for zircon U–Pb dating and trace elements compositions were performed by the software of ICPMSDataCal 8.3 (Liu et al., 2010b). The fixed integrating time of the measured signal is 38s for sample XTS-2 and 31s for sample ZJG-6. Common Pb was corrected following Andersen (2002). Concordia diagrams and weighted mean calculations were made using Isoplot/ver. 4.15 (Ludwig, 2003).

**Table 1**  
LA-ICPMS zircon U–Pb dating results of formation A-1 from the Tanjianshan Group.

Spot No.	Group	Isotope ratio						Apparent age (Ma)					
		$^{207}\text{Pb}/^{206}\text{Pb}$	$1\sigma$	$^{207}\text{Pb}/^{235}\text{U}$	$1\sigma$	$^{206}\text{Pb}/^{238}\text{U}$	$1\sigma$	$^{207}\text{Pb}/^{206}\text{Pb}$	$1\sigma$	$^{207}\text{Pb}/^{235}\text{U}$	$1\sigma$	$^{206}\text{Pb}/^{238}\text{U}$	$1\sigma$
XTS-2-1	1	0.0557	0.0016	0.5802	0.0167	0.0756	0.0009	442	65	465	11	470	6
XTS-2-2	1	0.0576	0.0023	0.6059	0.0242	0.0763	0.0012	515	78	481	15	474	7
XTS-2-3	1	0.0583	0.0012	0.6104	0.0126	0.0760	0.0007	542	51	484	8	472	4
XTS-2-4	1	0.0573	0.0016	0.6017	0.0165	0.0762	0.0006	505	61	478	10	473	4
XTS-2-5	1	0.0570	0.0017	0.5997	0.0186	0.0763	0.0009	493	67	477	12	474	6
XTS-2-6	1	0.0563	0.0017	0.5929	0.0189	0.0764	0.0008	465	70	473	12	475	5
XTS-2-7	2	0.0541	0.0017	0.5481	0.0172	0.0735	0.0007	375	69	444	11	457	4
XTS-2-8	1	0.0540	0.0016	0.5656	0.0170	0.0760	0.0010	370	67	455	11	472	6
XTS-2-9	3	0.0554	0.0016	0.5335	0.0153	0.0699	0.0007	428	63	434	10	436	4
XTS-2-10	3	0.0554	0.0014	0.5336	0.0147	0.0698	0.0006	427	57	434	10	435	4
XTS-2-11	3	0.0549	0.0015	0.5229	0.0141	0.0691	0.0007	408	55	427	9	431	4
XTS-2-12	3	0.0560	0.0016	0.5361	0.0159	0.0694	0.0009	453	60	436	10	433	5
XTS-2-13	2	0.0575	0.0019	0.5838	0.0182	0.0737	0.0011	511	68	467	12	458	7
XTS-2-14	3	0.0573	0.0017	0.5507	0.0162	0.0697	0.0007	505	60	445	11	434	4
XTS-2-15	1	0.0557	0.0016	0.5833	0.0157	0.0760	0.0009	441	56	467	10	472	5
XTS-2-16	1	0.0603	0.0012	0.6335	0.0199	0.0762	0.0008	615	36	498	12	473	5
XTS-2-17	2	0.0604	0.0016	0.6124	0.0165	0.0735	0.0007	619	57	485	10	457	4
XTS-2-18	3	0.0575	0.0013	0.5508	0.0129	0.0695	0.0006	509	50	446	8	433	4
XTS-2-19	2	0.0585	0.0016	0.5846	0.0148	0.0725	0.0007	548	59	467	10	451	4
XTS-2-20	1	0.0572	0.0014	0.6005	0.0154	0.0762	0.0010	498	54	478	10	473	6
XTS-2-21	2	0.0585	0.0016	0.5963	0.0169	0.0739	0.0008	548	61	475	11	460	5
XTS-2-22	3	0.0548	0.0037	0.5277	0.0135	0.0698	0.0011	405	151	430	8	435	7
XTS-2-23	3	0.0579	0.0014	0.5512	0.0134	0.0691	0.0007	526	50	446	9	431	4
XTS-2-24	1	0.0570	0.0017	0.5957	0.0186	0.0758	0.0011	492	65	475	12	471	6
XTS-2-25	3	0.0578	0.0016	0.5520	0.0156	0.0693	0.0007	523	61	446	10	432	4
XTS-2-26	3	0.0574	0.0014	0.5505	0.0139	0.0696	0.0007	507	54	445	9	434	4
XTS-2-27	2	0.0601	0.0018	0.6079	0.0199	0.0733	0.0009	608	69	482	13	456	5
XTS-2-28	3	0.0577	0.0018	0.5543	0.0175	0.0697	0.0008	517	52	448	11	434	5
XTS-2-29	2	0.0553	0.0041	0.5608	0.0151	0.0735	0.0009	425	121	452	11	457	5
ZJG-6-1	2	0.0551	0.0025	0.5277	0.0236	0.0695	0.0013	416	89	430	15	433	8
ZJG-6-2	1	0.0538	0.0026	0.5427	0.0264	0.0732	0.0010	364	78	440	16	455	6
ZJG-6-3	1	0.0631	0.0022	0.6344	0.0229	0.0729	0.0009	713	68	499	14	454	5
ZJG-6-4	1	0.0574	0.0024	0.5828	0.0250	0.0737	0.0010	506	91	466	16	458	6
ZJG-6-5	1	0.0601	0.0027	0.6089	0.0276	0.0735	0.0011	606	95	483	17	457	7
ZJG-6-6	1	0.0560	0.0025	0.5546	0.0339	0.0718	0.0009	451	123	448	20	447	5
ZJG-6-7	1	0.0585	0.0031	0.5817	0.0282	0.0721	0.0010	549	109	466	18	449	6
ZJG-6-8	1	0.0571	0.0021	0.5806	0.0230	0.0737	0.0010	494	97	465	14	458	6
ZJG-6-9	2	0.0563	0.0033	0.5406	0.0225	0.0696	0.0014	463	111	439	14	434	8
ZJG-6-10	1	0.0523	0.0026	0.5301	0.0260	0.0735	0.0011	298	114	432	17	457	7
ZJG-6-11	1	0.0608	0.0033	0.6174	0.0361	0.0737	0.0012	632	93	488	21	458	7
ZJG-6-12	1	0.0577	0.0026	0.5769	0.0265	0.0725	0.0010	517	98	462	17	451	6
ZJG-6-13	2	0.0590	0.0026	0.5706	0.0239	0.0702	0.0013	567	101	458	17	437	8
ZJG-6-14	1	0.0576	0.0029	0.5806	0.0304	0.0731	0.0011	513	140	465	19	455	7
ZJG-6-15	1	0.0522	0.0024	0.5207	0.0246	0.0724	0.0012	294	106	426	16	451	7
ZJG-6-16	1	0.0597	0.0051	0.6045	0.0401	0.0734	0.0014	594	169	480	25	457	8
ZJG-6-17	1	0.0540	0.0025	0.5385	0.0249	0.0723	0.0010	369	128	437	16	450	6
ZJG-6-18	2	0.0565	0.0026	0.5441	0.0237	0.0698	0.0009	471	97	441	16	435	6
ZJG-6-19	2	0.0580	0.0037	0.5606	0.0269	0.0701	0.0013	528	130	452	15	437	8
ZJG-6-20	2	0.0556	0.0030	0.5361	0.0234	0.0699	0.0016	435	103	436	15	436	7
ZJG-6-21	1	0.0580	0.0025	0.5744	0.0236	0.0718	0.0010	528	112	461	16	447	6
ZJG-6-22	2	0.0537	0.0026	0.5172	0.0240	0.0698	0.0010	358	94	423	15	435	5
ZJG-6-23	1	0.0588	0.0029	0.5942	0.0279	0.0733	0.0011	559	106	474	18	456	7
ZJG-6-24	2	0.0576	0.0037	0.5539	0.0223	0.0697	0.0011	514	133	448	14	434	7

## 5. Results

### 5.1. CL images

CL images for representative analyzed zircon grains are illustrated in Fig. 4. Zircons in sample XTS-2 are almost colorless in transmitted light microscopy, except for some grains having a light-brown hue. Crystal lengths are 50–100 µm, with aspect ratios (length/width) ranging from 1:1 to 2:1 (Fig. 4a). Short prismatic forms dominate most crystals, followed by pyramid and equiaxed forms. These features are consistent with those of zircons from calc-alkaline magmatic rocks (Wang and Kienast, 1999). Most crystals display apparent euhedral crystal morphology, although most crystals were broken during the mineral separation process. Concentric oscillatory zoning (comparable broad bright-CL and narrow black-CL zones) is clear for the majority of zircon crystals, indicative of growth from magma (Hoskin, 2000). In addition, some crystals have thin discrete CL-bright rims and a few crystals show one or several marked thin dark-CL rings against broad grey-CL zonings and little black patches in cores (Fig. 4a). On the other hand, zircons from sample ZJG-6 have hardly any intact crystal forms, but still preserve the euhedral outline (Fig. 4b). Most grains have long axes varying from 50 to 100 µm, with aspect ratios from 1:1 to 2:1. Oscillatory zoning is clearly indicative of magmatic origin, but the discrete bright-CL rims, irregular bright-CL areas and bright-CL micro-fractures crosscutting the zircons are also very obvious (Fig. 4b). In addition, the widths of dark-CL rings within some zircons are also elevated. Though the zircons from sample XTS-2 are mostly darker than the zircons from sample ZJG-6 in CL images, they possess more regular internal textures. In summary, although the original magmatic oscillatory zoning remains clear and distinguishable for these two samples, evidence of overprinting by hydrother-

mal/metamorphic fluids is obvious, especially for the zircons from sample ZJG-6.

### 5.2. Zircon U–Pb ages

Zircon LA-ICPMS U–Pb dating results for XTS-2 and ZJG-6 are presented in Table 1. Twenty-nine U–Pb isotopic analyses were performed for sample XTS-2 with concordance >90%. The  $^{206}\text{Pb}/^{238}\text{U}$  ages of sample XTS-2 range from 475 to 431 Ma, and three age groups can be distinguished, i.e., 475–470 Ma, 460–451 Ma, and 436–431 Ma (Table 1). Eleven spots from the first group of sample XTS-2 yielded a concordant U–Pb age of  $472.7 \pm 3.3$  Ma (MSWD = 0.07) and a mean  $^{206}\text{Pb}/^{238}\text{U}$  age of  $472.8 \pm 3.1$  Ma (MSWD = 0.06) (Fig. 5a). Another seven spots from the second age group of this sample yielded a concordant U–Pb age of  $456.7 \pm 4.4$  Ma (MSWD = 0.42) and a mean age of  $456.3 \pm 3.4$  Ma (MSWD = 0.38) (Fig. 5b). The second age group comprises eleven spots which yielded a concordant U–Pb age of  $433.8 \pm 3.5$  Ma (MSWD = 0.16) and a mean age of  $433.2 \pm 2.5$  Ma (MSWD = 0.16) (Fig. 5c). On the other hand, twenty-four U–Pb isotopic analyses were conducted for sample ZJG-6 with concordance >90% and  $^{206}\text{Pb}/^{238}\text{U}$  ages ranging from 458 to 433 Ma (Table 1). Two age groups can be differentiated from this sample. i.e., 458–447 Ma and 437–433 Ma. Sixteen spots from the first age group of sample ZJG-6 yielded a concordant U–Pb age of  $453.1 \pm 3.4$  Ma (MSWD = 0.46) and a mean  $^{206}\text{Pb}/^{238}\text{U}$  age of  $453.3 \pm 3.1$  Ma (MSWD = 0.46) (Fig. 5d). The last age group is composed of eight spots which yielded a concordant U–Pb age of  $434.7 \pm 5.7$  Ma (MSWD = 0.03) and a mean age of  $435.1 \pm 4.8$  Ma (MSWD = 0.03) (Fig. 5e). Thus, the two samples have similar age ranges and variations, consistent with the previous reports of 463–458 Ma (Liang et al., 2014) and 454–451 (Fu et al., 2017), but also show a younger age population of 440–430 Ma for Formation A-1 of the Tanjianshan Group (Fig. 5f).

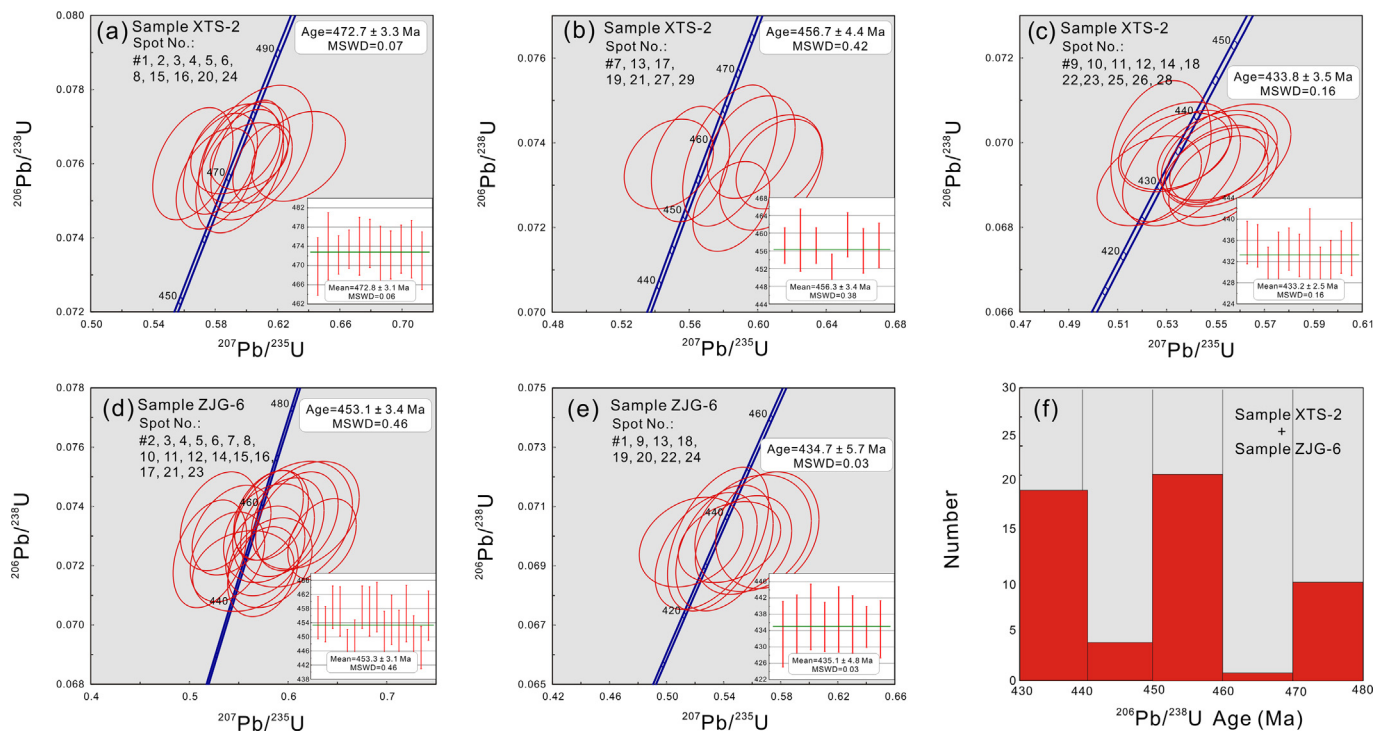


Fig. 5. Zircon U–Pb dating results for sample XTS-2 (a–c), sample ZJG-6 (d, e) and all zircon analyses combined (f). Concordia plots were processed using ISOPLOT 4.15 (Ludwig, 2003). The U–Pb ages were calculated at  $2\sigma$  level in the Concordia plots. Data-point error symbols (error bars) in all inset diagrams are  $1\sigma$ .

**Table 2**

LA-ICPMS zircon element results of formation A-1 from the Tanjianshan Group (ppm).

Spot No.	Group	La	Ce	Pr	Nd	Sm	Eu	Gd	Tb	Dy	Ho	Er	Tm	Yb	Lu	$\Sigma$ REE	LREE
XTS-2-1	1	0.06	13.5	0.14	2.00	3.30	0.49	21.3	7.4	105	44.7	228	54.8	614	124	1219	19.5
XTS-2-2	1	0.05	16.2	0.05	0.34	2.21	0.33	13.3	5.5	81	35.4	187	45.9	539	106	1032	19.2
XTS-2-3	1	0.08	21.2	0.05	1.51	2.61	0.29	18.4	6.8	98	41.6	215	52.1	587	115	1161	25.7
XTS-2-4	1	0.07	13.6	0.02	1.05	1.65	0.23	12.2	4.5	65	27.9	148	36.0	416	83	809	16.6
XTS-2-5	1	0.06	12.8	0.01	0.84	1.88	0.46	12.1	4.7	67	30.1	163	40.5	467	95	895	16.0
XTS-2-6	1	0.09	19.1	0.03	1.19	2.23	0.38	18.7	7.0	97	42.0	219	53.2	599	116	1175	23.0
XTS-2-7	2	0.06	14.9	0.06	1.73	4.01	0.46	21.9	8.1	113	46.7	239	56.7	623	123	1252	21.3
XTS-2-8	1	0.13	12.1	0.01	0.51	1.56	0.28	10.3	4.1	58	25.4	135	32.7	368	73	722	14.6
XTS-2-9	3	1.06	18.2	0.36	1.97	2.06	0.37	12.9	5.7	78	33.7	176	43.7	493	97	964	24.1
XTS-2-10	3	0.51	14.3	0.17	1.80	1.85	0.34	11.2	4.4	65	28.1	148	37.0	419	83	815	19.0
XTS-2-11	3	0.83	15.3	0.20	1.06	2.24	0.30	11.7	5.0	75	34.3	186	47.1	543	111	1033	19.9
XTS-2-12	3	0.67	13.3	0.04	1.40	1.84	0.31	13.2	5.3	72	31.6	167	40.3	453	95	894	17.6
XTS-2-13	2	0.07	13.0	0.02	0.61	2.34	0.23	13.4	5.5	77	34.9	180	45.1	518	103	994	16.3
XTS-2-14	3	0.12	24.3	0.13	1.55	3.07	0.43	22.1	8.1	111	47.3	238	56.6	626	121	1260	29.6
XTS-2-15	1	0.07	13.2	0.02	0.62	2.21	0.57	13.8	5.5	81	35.6	190	46.8	535	108	1032	16.7
XTS-2-16	1	0.09	16.4	0.09	1.22	2.08	0.51	14.9	5.8	82	35.9	188	46.6	532	108	1034	20.4
XTS-2-17	2	0.06	17.8	0.08	1.04	2.90	0.51	20.3	7.4	104	44.2	231	55.9	623	119	1227	22.4
XTS-2-18	3	1.37	46.5	1.60	10.7	11.8	2.34	47.2	16.5	212	83.6	409	95.2	1040	194	2171	74.3
XTS-2-19	2	0.05	20.1	0.01	0.95	2.75	0.46	18.7	7.1	96	41.6	211	51.3	569	112	1132	24.4
XTS-2-20	1	0.02	13.0	0.01	0.35	1.78	0.39	12.6	4.6	69	30.5	165	41.4	482	95	916	15.5
XTS-2-21	2	0.10	19.7	0.06	1.28	3.52	0.49	21.5	7.8	112	48.6	254	61.8	704	137	1372	25.2
XTS-2-22	3	33.80	82.7	8.60	39.1	10.1	1.12	32.6	10.0	122	51.4	267	62.1	677	135	1531	175.3
XTS-2-23	3	2.55	19.3	0.62	3.40	2.43	0.31	11.9	4.9	68	29.7	159	38.7	441	89	871	28.6
XTS-2-24	1	0.03	19.6	0.08	1.17	2.62	0.34	16.4	6.7	96	41.8	221	53.9	622	123	1204	23.8
XTS-2-25	3	0.51	14.1	0.08	0.66	1.70	0.27	11.9	4.6	67	29.5	158	38.6	453	90	870	17.4
XTS-2-26	3	0.85	16.5	0.30	1.95	2.63	0.51	16.8	6.3	87	38.7	207	50.6	581	118	1128	22.8
XTS-2-27	2	0.13	16.8	0.03	1.40	2.50	0.34	15.9	6.3	92	40.2	214	53.2	601	123	1166	21.2
XTS-2-28	3	8.05	35.3	2.73	13.9	5.9	0.56	22.0	7.5	104	45.3	236	56.3	632	125	1294	66.5
XTS-2-29	2	0.02	16.0	0.10	2.66	4.67	0.65	28.4	10.5	143	58.8	297	69.8	764	152	1548	24.1
ZJG-6-1	2	4.02	26.1	1.25	7.91	5.87	1.21	25.9	9.3	130	52.6	289	64.4	769	146	1532	46.4
ZJG-6-2	1	0.31	16.1	0.20	1.86	3.02	0.59	15.9	5.4	86	35.8	204	47.7	591	113	1120	22.1
ZJG-6-3	1	0.18	15.9	0.24	3.33	5.55	1.12	31.0	10.0	141	55.2	294	62.7	713	131	1464	26.4
ZJG-6-4	1	0.04	10.7	0.03	0.52	1.41	0.22	10.9	3.9	62	27.1	158	37.6	468	94	873	12.9
ZJG-6-5	1	0.04	16.4	0.09	1.59	3.51	0.56	20.2	7.6	110	45.2	258	57.4	704	134	1359	22.2
ZJG-6-6	1	0.48	17.0	0.57	2.85	3.30	0.86	14.6	5.1	81	34.3	180	40.0	477	89	946	25.0
ZJG-6-7	1	0.23	9.6	0.13	1.03	1.86	0.42	10.6	4.0	63	26.2	156	37.1	458	89	857	13.2
ZJG-6-8	1	0.79	23.4	0.80	6.68	6.78	1.70	30.6	11.0	152	60.1	329	74.3	882	164	1744	40.1
ZJG-6-9	2	3.43	51.3	2.95	16.9	8.40	2.62	33.9	11.0	146	58.0	309	67.2	789	147	1646	85.6
ZJG-6-10	1	0.01	16.2	0.07	1.28	3.14	0.66	23.1	8.2	122	51.9	279	63.9	769	138	1476	21.4
ZJG-6-11	1	0.16	13.7	0.14	2.48	4.05	0.86	23.1	7.7	114	46.4	240	52.8	625	113	1244	21.4
ZJG-6-12	1	1.17	10.2	0.36	1.75	1.97	0.33	12.1	4.5	68	28.5	159	38.2	468	89	882	15.7
ZJG-6-13	2	1.81	25.6	1.43	8.07	6.22	2.03	24.9	8.1	114	45.4	251	57.0	674	126	1346	45.2
ZJG-6-14	1	0.31	11.7	0.16	1.93	2.81	0.59	14.0	4.2	66	26.1	148	34.1	416	78	804	17.5
ZJG-6-15	1	0.05	13.7	0.09	0.99	2.36	0.55	15.0	5.6	92	38.5	218	49.1	591	112	1139	17.8
ZJG-6-16	1	0.02	10.7	0.03	0.96	2.49	0.46	14.2	5.4	82	36.5	204	49.9	594	115	1115	14.7
ZJG-6-17	1	0.02	10.0	0.05	0.96	2.03	0.50	14.1	4.9	77	32.9	179	41.8	502	97	962	13.6
ZJG-6-18	2	4.73	25.5	1.65	8.01	3.64	0.66	16.2	5.7	83	33.9	188	43.4	517	97	1028	44.2
ZJG-6-19	2	5.34	34.5	2.80	17.0	11.9	3.23	44.3	13.9	177	66.8	346	76.4	886	161	1846	74.7
ZJG-6-20	2	6.49	31.8	2.75	18.4	15.7	4.96	57.9	17.7	212	79.2	388	83.5	973	175	2066	80.2
ZJG-6-21	1	0.02	9.1	0.05	1.28	3.05	0.66	16.8	5.9	83	34.1	184	41.7	494	93	967	14.1
ZJG-6-22	2	1.80	15.5	0.81	3.36	3.45	0.61	17.4	6.1	90	37.8	212	48.0	577	109	1123	25.5
ZJG-6-23	1	0.02	10.7	0.04	1.03	1.95	0.43	12.8	4.9	74	32.5	190	45.1	565	112	1050	14.2
ZJG-6-24	2	2.59	21.0	1.09	4.57	4.62	0.81	16.6	5.9	90	37.5	212	48.7	597	119	1161	34.7
Spot No.	Group	HREE	LREE/HREE	Eu/Eu <sup>*</sup>	Ce/Ce <sup>*</sup>	Pb	Th	U	Y	Hf	Ta	Nb	Ti	Th/U	Nb/Ta	Hf/Y	T <sub>Ti</sub> (°C)
XTS-2-1	1	1199	0.02	0.13	25.28	55	199	298	1441	10766	0.78	2.02	5.93	0.67	2.59	7.47	699
XTS-2-2	1	1012	0.02	0.14	68.54	60	219	345	1150	11087	1.10	2.59	4.17	0.64	2.35	9.65	670
XTS-2-3	1	1135	0.02	0.09	85.06	124	465	503	1360	10152	1.31	3.88	6.38	0.92	2.96	7.46	705
XTS-2-4	1	793	0.02	0.11	100.57	53	182	294	925	11365	0.85	1.95	3.21	0.62	2.30	12.29	649
XTS-2-5	1	879	0.02	0.22	107.62	43	144	251	1000	10747	0.87	2.28	5.97	0.58	2.61	10.74	699
XTS-2-6	1	1152	0.02	0.12	91.08	79	288	372	1348	11064	1.14	3.23	4.79	0.77	2.83	8.21	681
XTS-2-7	2	1231	0.02	0.12	59.61	55	195	284	1477	10478	0.82	2.52	3.49	0.69	3.08	7.09	656
XTS-2-8	1	707	0.02	0.16	63.81	40	139	233	820	10450	0.71	1.82	4.45	0.60	2.57	12.74	675
XTS-2-9	3	940	0.03	0.17	7.21	64	237	349	1096	11422	1.05	2.33	3.34	0.68	2.21	10.42	652
XTS-2-10	3	796	0.02	0.18	11.85	51	171	281	926	11262	0.84	1.78	6.74	0.61	2.12	12.16	710
XTS-2-11	3	1013	0.02	0.15	8.98	46	149	280	1133	10539	1.22	3.02	4.98	0.53	2.48	9.31	684
XTS-2-12	3	877	0.02	0.14	13.60	49	155	264	1021	9360	1.02	2.09	2.32	0.59	2.04	9.17	625
XTS-2-13	2	977	0.02	0.10	80.58	53	176	278	1113	10543	0.91	2.14	3.33	0.63	2.35	9.47	652
XTS-2-14	3	1230	0.02	0.12	42.76	123	398										

**Table 2** (continued)

Spot No.	Group	HREE	LREE/HREE	Eu/Eu <sup>*</sup>	Ce/Ce <sup>*</sup>	Pb	Th	U	Y	Hf	Ta	Nb	Ti	Th/U	Nb/Ta	Hf/Y	T <sub>ri</sub> (°C)
XTS-2-20	1	900	0.02	0.19	226.20	48	162	282	1005	10871	0.94	2.42	6.19	0.57	2.57	10.82	703
XTS-2-21	2	1347	0.02	0.13	59.28	84	288	405	1578	10031	1.17	3.68	8.84	0.71	3.14	6.36	734
XTS-2-22	3	1356	0.13	0.17	1.16	61	219	301	1656	10021	0.79	2.19	5.98	0.73	2.76	6.05	700
XTS-2-23	3	842	0.03	0.14	3.66	62	201	300	973	10236	0.92	2.42	4.93	0.67	2.62	10.52	683
XTS-2-24	1	1180	0.02	0.12	61.86	79	291	409	1359	11076	1.22	3.52	5.64	0.71	2.89	8.15	695
XTS-2-25	3	852	0.02	0.13	15.10	53	193	301	964	11050	0.98	2.05	5.01	0.64	2.10	11.46	685
XTS-2-26	3	1106	0.02	0.18	8.03	63	216	338	1276	10287	1.51	3.08	6.18	0.64	2.04	8.07	702
XTS-2-27	2	1145	0.02	0.12	68.33	66	235	365	1323	11136	1.20	3.15	4.94	0.64	2.62	8.42	684
XTS-2-28	3	1228	0.05	0.13	1.84	65	196	312	1450	10662	1.04	2.91	44.48	0.63	2.80	7.36	908
XTS-2-29	2	1524	0.02	0.13	46.65	89	268	358	1873	10863	0.82	2.06	4.72	0.75	2.50	5.80	680
ZJG-6-1	2	1486	0.03	0.25	2.83	186	341	464	1888	9611	0.86	2.61	6.14	0.74	3.05	5.09	702
ZJG-6-2	1	1098	0.02	0.21	15.48	143	234	351	1291	9834	0.69	2.73	12.53	0.67	3.96	7.62	767
ZJG-6-3	1	1438	0.02	0.21	15.92	132	267	342	1897	9762	0.65	2.02	5.76	0.78	3.10	5.15	696
ZJG-6-4	1	860	0.01	0.12	66.87	65	118	238	983	9603	0.70	1.95	4.49	0.49	2.77	9.77	676
ZJG-6-5	1	1337	0.02	0.16	47.79	161	304	413	1660	9708	0.72	2.51	5.58	0.74	3.48	5.85	694
ZJG-6-6	1	921	0.03	0.32	6.93	98	206	319	1130	9534	0.70	2.26	2.57	0.65	3.24	8.44	632
ZJG-6-7	1	843	0.02	0.23	13.30	54.6	108	215	970	9815	0.58	1.75	3.46	0.50	3.04	10.11	655
ZJG-6-8	1	1704	0.02	0.30	6.51	237	415	511	2188	9524	0.78	2.88	8.14	0.81	3.67	4.35	727
ZJG-6-9	2	1561	0.05	0.41	3.69	228	434	562	2011	8613	1.08	4.11	7.04	0.77	3.80	4.28	714
ZJG-6-10	1	1455	0.01	0.17	69.60	150	273	385	1814	10496	0.79	2.18	7.61	0.71	2.77	5.79	721
ZJG-6-11	1	1222	0.02	0.21	20.76	119	212	277	1575	9463	0.69	2.07	6.79	0.77	3.00	6.01	711
ZJG-6-12	1	866	0.02	0.16	3.83	60	107	201	1031	9673	0.47	0.91	3.64	0.53	1.95	9.38	659
ZJG-6-13	2	1301	0.03	0.43	3.69	165	296	355	1633	9656	0.79	2.44	4.03	0.83	3.11	5.91	667
ZJG-6-14	1	787	0.02	0.23	12.44	90	185	239	943	9816	0.47	1.63	11.70	0.78	3.45	10.41	761
ZJG-6-15	1	1121	0.02	0.21	37.93	97	190	305	1367	9457	0.75	2.16	7.21	0.62	2.88	6.92	716
ZJG-6-16	1	1101	0.01	0.18	95.10	93	162	293	1304	10023	0.71	1.80	6.30	0.55	2.54	7.69	704
ZJG-6-17	1	948	0.01	0.21	55.16	67	127	227	1143	9728	0.63	1.67	9.55	0.56	2.66	8.51	741
ZJG-6-18	2	984	0.04	0.22	2.23	109	190	289	1214	9780	0.75	2.19	10.84	0.66	2.93	8.06	753
ZJG-6-19	2	1771	0.04	0.38	2.16	281	490	541	2328	9563	1.04	2.79	20.39	0.91	2.67	4.11	817
ZJG-6-20	2	1985	0.04	0.44	1.85	273	538	617	2649	8738	0.76	2.58	5.56	0.87	3.41	3.30	693
ZJG-6-21	1	953	0.01	0.22	48.50	74	138	206	1201	8822	0.38	1.35	189.23	0.67	3.58	7.34	1125
ZJG-6-22	2	1097	0.02	0.20	3.14	78	159	244	1350	9925	0.59	1.48	2.81	0.65	2.49	7.35	639
ZJG-6-23	1	1036	0.01	0.20	62.04	70	125	250	1174	10009	0.79	1.97	4.67	0.50	2.50	8.53	679
ZJG-6-24	2	1126	0.03	0.25	3.06	106	229	347	1318	8822	0.76	2.62	3.88	0.66	3.46	6.69	664

### 5.3. Trace and rare earth elements

Zircon LA-ICPMS trace and rare earth element analytical results for the two samples XTS-2 and ZJG-6 are presented in Table 2. For REEs, zircons from these two samples are generally enriched in HREE and depleted in LREE, with marked positive Ce but negative Eu anomalies (Fig. 6). Nevertheless, it is notable that REE concentrations are variable between zircon groups with different ages. For sample XTS-2, age group 1 zircons (475–470 Ma) and age group 2 zircons (459–451 Ma) have similar concentrations of REE and almost identical REE patterns, with significant enrichment of HREE (LREE/HREE = 0.02), pronounced positive Ce anomalies ( $Ce/Ce^* = 25.28\text{--}226.20$ ) and moderate negative Eu anomalies ( $Eu/Eu^* = 0.09\text{--}0.24$ ) (Fig. 6a). In contrast, age group 3 zircons

(436–431 Ma) from sample XTS-2 have much higher concentrations of LREE (LREE/HREE = 0.02–0.13), less pronounced positive Ce anomalies ( $Ce/Ce^* = 1.16\text{--}42.76$ ) and Eu anomalies ( $Eu/Eu^* = 0.12\text{--}0.26$ ) relative to groups 1 and 2 (Fig. 6a). REE patterns from sample ZJG-6 have similar variations as in sample XTS-2: more enrichment of HREE (LREE/HREE = 0.01–0.03), more pronounced positive Ce ( $Ce/Ce^* = 3.83\text{--}95.10$ ) and negative Eu anomalies ( $Eu/Eu^* = 0.12\text{--}0.32$ ) for the older age group 1 zircons (458–446 Ma) whereas higher compositions of LREE (LREE/HREE = 0.02–0.05), less pronounced Ce ( $Ce/Ce^* = 1.85\text{--}3.69$ ) and Eu anomalies ( $Eu/Eu^* = 0.20\text{--}0.44$ ) for the younger age group 2 zircons (437–433 Ma) (Fig. 6b). In summary, REE variations are consistent with the age variations for both samples from Formation A-1 of the Tanjianshan Group.

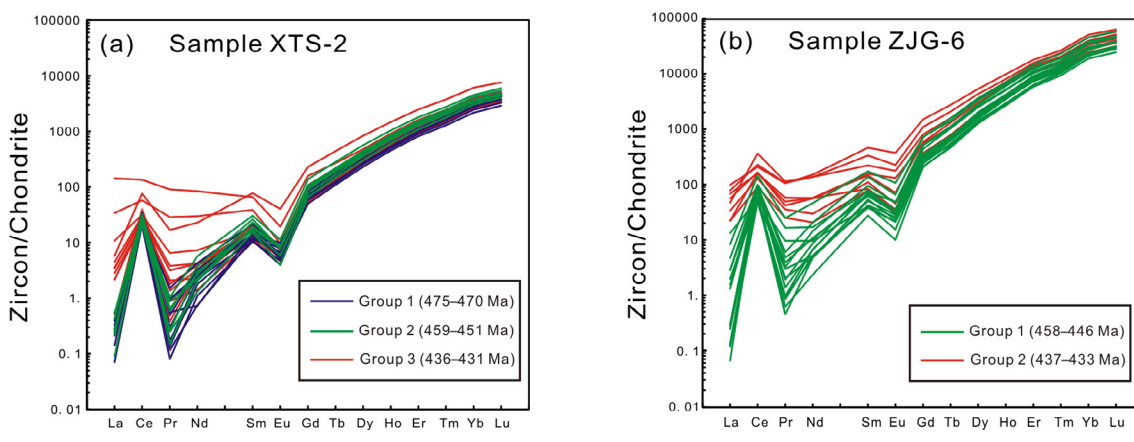
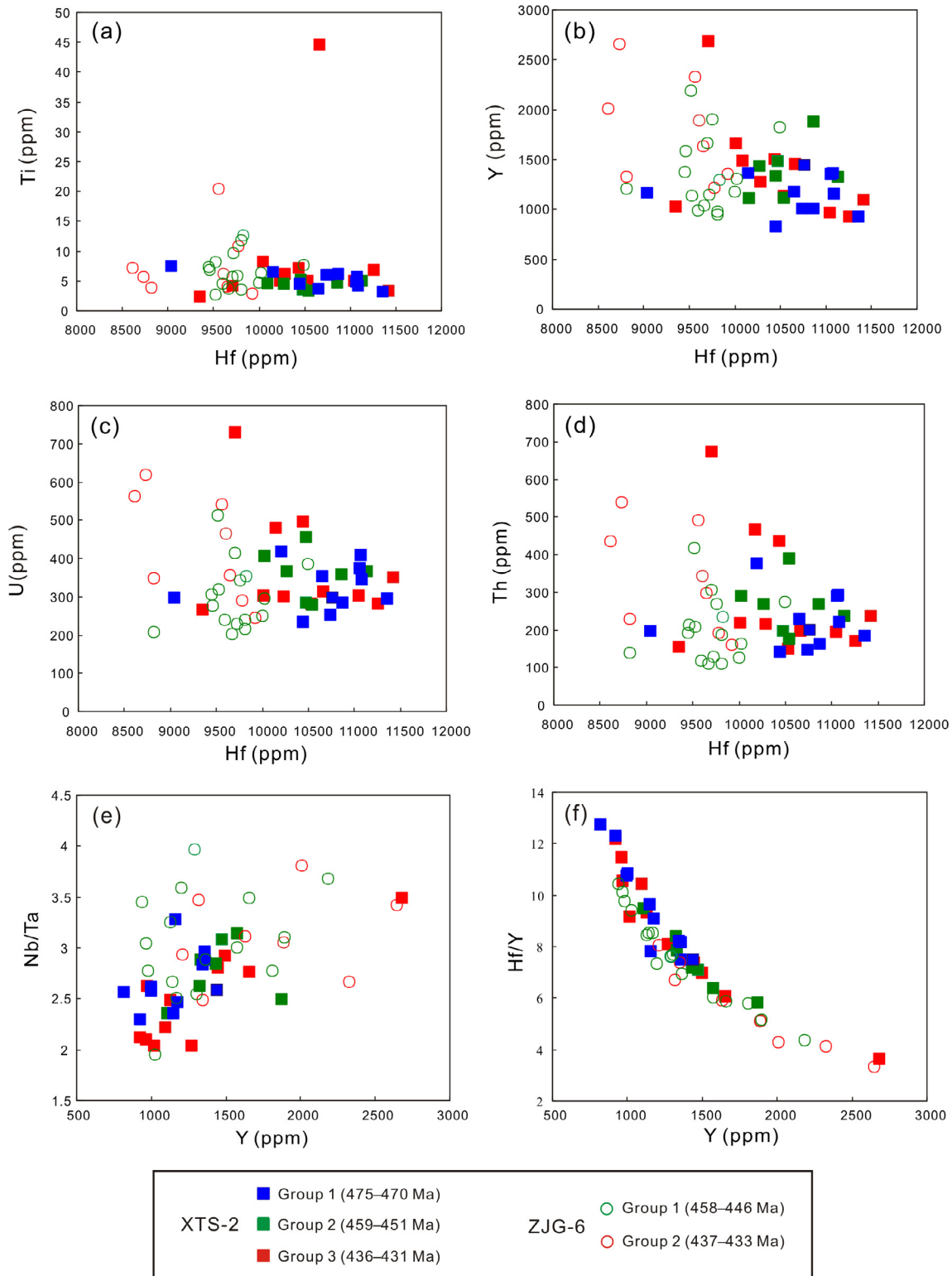


Fig. 6. Chondrite-normalized REE patterns for zircons from samples XTS-2 (a) and ZJG-6 (b).



**Fig. 7.** Plots of (a) Hf vs. Ti, (b) Hf vs. Y, (c) Hf vs. U, (d) Hf vs. Th, (e) Y vs. Nb/Ta, and (f) Y vs. Hf/Y for zircons from samples XTS-2 and ZJG-6.

Other trace elements are also variable between different samples and age groups (Fig. 7). The Th/U ratios are 0.53–0.92 for XTS-2 zircons and 0.49–0.91 for ZJG-6 zircons. Compared to XTS-2 zircons, ZJG-6 zircons possess lower Hf contents (mostly <10000 ppm) but slightly higher and more variable concentrations of Ti (2.57–20.4 ppm; Fig. 7a), Y (943–2649 ppm; Fig. 7b), U (201–617 ppm; Fig. 7c) and Th (107–538 ppm; Fig. 7d). Zircons from

sample ZJG-6 also have higher average ratios of Nb/Ta (Fig. 7e) but lower Hf/Y (Fig. 7f), compared to XTS-2 zircons. All of this suggests some degree of fluid modification. In addition, the younger age groups from both samples have higher concentrations of Y (Fig. 7b), U (Fig. 7c) and Th (Fig. 7d) compared to the older age groups, implying that the younger zircon crystals were affected by fluids.

## 6. Discussion

### 6.1. Zircon crystallization temperatures

Ferry and Waston (2007) documented that the Ti content of zircon coexisting with rutile and either quartz or zirconia has a significant dependence on temperature. In the case of low  $\alpha_{\text{SiO}_2}$  activity ( $\alpha_{\text{SiO}_2}$ ), Ti will more strongly substitute for Si in zircon at the same temperature, whereas in the case of high  $\alpha_{\text{SiO}_2}$  (e.g. at quartz saturation), less Ti substitutes for Si resulting in a lower Ti content. At high  $\alpha_{\text{SiO}_2}$  conditions, substantiated by the presence of quartz and consistent with silica-saturated ryholitic dacite or dacite compositions, no corrections for the Ti-in-zircon thermometer are required.

However, the Ti content of zircon is affected by the rutile saturation level in the melt at a given temperature ( $T$ ) (Troitzsch et al., 2004; Watson and Harrison, 2005; Watson et al., 2006; Ferry and Waston, 2007). Watson et al. (2006) fitted an equation based on experiment and natural zircon data to express the relationship between the Ti content of zircon coexisting with rutile and/or quartz and  $T$  (i.e., Ti-in-zircon thermometer). Ferry and Waston (2007) further calibrated the equation proposed by Watson et al. (2006) to accommodate the calculation of Ti content in zircon without the presence of rutile and/or quartz or for use when constrained data of  $\alpha_{\text{SiO}_2}$  and  $\alpha_{\text{TiO}_2}$  (activity of  $\text{TiO}_2$ ) is lacking. They documented that the maximum uncertainty on  $T$  obtained using the calibrated equation is, under the conditions of unconstrained  $\alpha_{\text{SiO}_2}$  and  $\alpha_{\text{TiO}_2}$ , less than 50 °C at 750 °C and ±1 GPa.

For samples XTS-2 and ZJG-6, rutile grains are not observed under the microscope; thus it is not clear whether they are present in the volcanic rocks. Nevertheless, the Ti-in-zircon thermometer is able to constrain the minimum temperature of zircon crystallization. Given  $\alpha_{\text{TiO}_2} = 1$  and  $\alpha_{\text{SiO}_2} = 1$ , the crystallization temperatures of zircon ( $T_{\text{Ti}}$  °C) were calculated for the two samples (XTS-2 and ZJG-6) (Table 2). Temperatures vary from 600 to 750 °C, except for the three Ti-anomalous zircons (XTS-2-28, ZJG-6-19 and ZJG-6-21) that yielded temperatures from 800 to 1125 °C. These anomaly high Ti values could be attributed to fluid/mineral inclusions intersected during LA-ICPMS analysis, which manifest as short duration Ti spikes in time resolved analysis. The crystallization temperatures obtained in this study are close to the lower temperature range triggering felsic melt formation beneath a continental margin arc (Carley et al., 2014).

### 6.2. Timing of metamorphism in the Tanjianshan Group

Zircon U-Pb ages broadly fall into three groups: 475–470 Ma, 460–450 Ma, and 440–430 Ma. The older age populations are consistent with those previously reported (Zhao et al., 2003; Liang et al., 2014; Fu, 2015; Fu et al., 2017). However, the youngest age group (i.e., 440–430 Ma) was not previously detected. In context of the regional geological background, the time span of subduction between the South Qilian Ocean and Qilian block in the early Paleozoic in the NMQB has recently been dated as 540–460 Ma (Xiong et al., 2014). The younger age population (440–430 Ma) reported in this study is, therefore, more likely to reflect metamorphism than volcanism. An essential question, however, is whether the metamorphic grade of epidote-amphibolite to amphibolite facies could reset the zircon U-Pb isotopic chronometer in the Tanjianshan Group. Based on the analysis of micro metamorphic and deformed features, CL-images, trace and rare earth elements and Ti-in-zircon thermometry, the following evidence suggests that metamorphic resetting did occur:

- (1) The metacrust mineral assemblages in both samples are plagioclase + muscovite + epidote + quartz for felsic components and hornblende (locally chloritization) + plagioclase

+ epidote + quartz for andesitic components. Considering the coexistence of muscovite and quartz without orthoclase in the felsic rocks, it can be concluded that the metamorphic grade of the volcanic rocks should vary from epidote-amphibolite to amphibolite facies, broadly equivalent to a temperature range from 550 to 650 °C in the setting of orogenic thickened crust (Chalokwu, 1989).

- (2) There are intensive quartz ribbons without strain observed under the microscope. This phenomenon was also observed in the quartzofeldspathic mylonite from the Schirmacher Hills, East Antarctica (Bose and Sengupta, 2003) and the Simplon Fault Zone in the central Alps (Mancktelow and Pennacchioni, 2004). It reveals physical conditions of deformation under high temperature in a water-rich environment and recrystallization of metacryst quartz by fast boundary migration (Mancktelow and Pennacchioni, 2004). In addition, some phenomena such as long axes of feldspar megaporphyroclasts being near perpendicular to foliation, quartz ribbons swerving symmetrically along the sides of feldspar mega-porphyroclasts, widths of quartz ribbons being controlled by widths of single quartz grains and high aspect ratios occurring for single quartz grains (Fig. 3n, o), indicate that deformation occurred in the late stage of quartzfeldspathic mylonitization under a high temperature conditions (600–650 °C, Bose and Sengupta, 2003).
- (3) Oscillatory zoning in zircon is indicative of a magmatic origin (Hoskin, 2000), while irregular zoning occurs commonly in zircons modified by metamorphic fluids (Gao et al., 2015). In addition, Hoskin and Black (2000) further studied the internal structure of zircon formed under the conditions of solid-state recrystallization, including blurred primary zones, convoluted zoning, transgressive recrystallization and recrystallization front. Moreover, Geisler et al. (2003) and Hoskin (2005) investigated the internal structure of zircon formed from hydrothermal alteration or hydrothermal deposition, and concluded that areas that suffered hydrothermal alteration commonly have dark-CL images, various irregular zoning, small dark patches, and infilling along microfractures and metamict crystal domains. Compared to the internal structures of zircons originating from solid-state recrystallization or hydrothermal alteration, most age group 1 (475–470 Ma) and group 2 (460–451 Ma) zircons from sample XTS-2 appear to have a magmatic origin, whereas age group 3 (436–431 Ma) zircons were probably influenced by metamorphism-related hydrothermal modification (as evidenced by their partially dark-CL images) or metamictization manifested by their partial blurred primary zonation (Fig. 4a). This is further supported by the age group 2 (437–433 Ma) zircons from sample ZJS-6, which show significant overprints of metamorphic activity, preserving primary zoning but also dark-CL images, and infilling or diffusion along microfractures and metamict areas (Fig. 4b). Compared to group 3 (436–431 Ma) zircons from sample XTS-2, the intensity of metamorphic reworking is significantly stronger for the group 2 (437–433 Ma) zircons from sample ZJG-6, which is also reflected in the greater losses of radioactive Pb and more discordant ages (Fig. 5e).
- (4) The relative enrichment of LREEs, less pronounced Ce anomalies and flat chondrite-normalized LREE curves are characteristics of zircons modified by metamorphism or hydrothermal alteration (Mathieu et al., 2001; Schmitt and Vazquez, 2006; Soman et al., 2010; Li et al., 2014, 2017; Liu et al., 2014). Zircons formed by solid-state recrystallization show LREE-depleted characteristic due to the lower compatibility of LREE relative to HREE and the preference

of LREE to partition into hydrothermal fluids during metamorphic processes (Schaltegger et al., 1999; Hoskin and Black, 2000). Moreover, zircons derived from magmatic or hydrothermal processes commonly possess concave-down HREEs patterns on chondrite-normalized curves, in contrast to the concave-up curves common in zircons that experienced solid-state recrystallization (Hoskin and Black, 2000). Accordingly, it is reasonable to classify the younger age groups (440–430 Ma) from the two samples as metamorphically modified zircons that underwent replacement recrystallization in the presence of a metamorphic fluid. These zircons have similar CL and geochemical characteristics as those reported in the Dabie Orogen (Xia et al., 2010), which underwent supercritical fluid modification during continental subduction-zone metamorphism. They plot in the metamorphic fluid alteration field on the zircon discriminant diagrams (Fig. 8a-d), which further hints at metamorphic fluid overprinting. On the other hand, the range of U and Th concentrations (one to hundreds ppm) and Th/U ratios (>0.5) in all zircon groups from the Xitieshan deposit are consistent with those derived from intermediate-acidic magmatic rocks (Wang et al., 2011). The good linear relationships between U and Th indicate a

significant fractionation-induced elemental covariation (Barth et al., 2013). Thus, it can be concluded that the older zircons (>450 Ma) reported in this study retain original fingerprints of magmatic fractionation, whereas the younger zircons (440–430 Ma) may have been overprinted and reset by metamorphic fluids.

- (5) Ti-in-zircon thermometry suggests that most zircons from both samples crystallized within a temperature range from 600 to 750 °C. This range partly overlaps the lower temperature range (550–650 °C) implied by metamorphic grade and microstructure deformation as mentioned above. It is reasonable, therefore that recrystallization and resetting of the zircon U-Pb chronometer occurred.

Collectively, we believe the younger zircon age population (440–430 Ma) records the timing of high temperature metamorphism-associated massive fluid activity during the orogeny in the Late Ordovician to Middle Silurian. Due to the relatively low crystallization temperature, the pristine magmatic zircons underwent different levels of overprinting and transformation, resulting in Pb loss and younging, as well as in microstructure deformation and development of characteristic metamorphic mineral assemblages in the volcanic rocks.

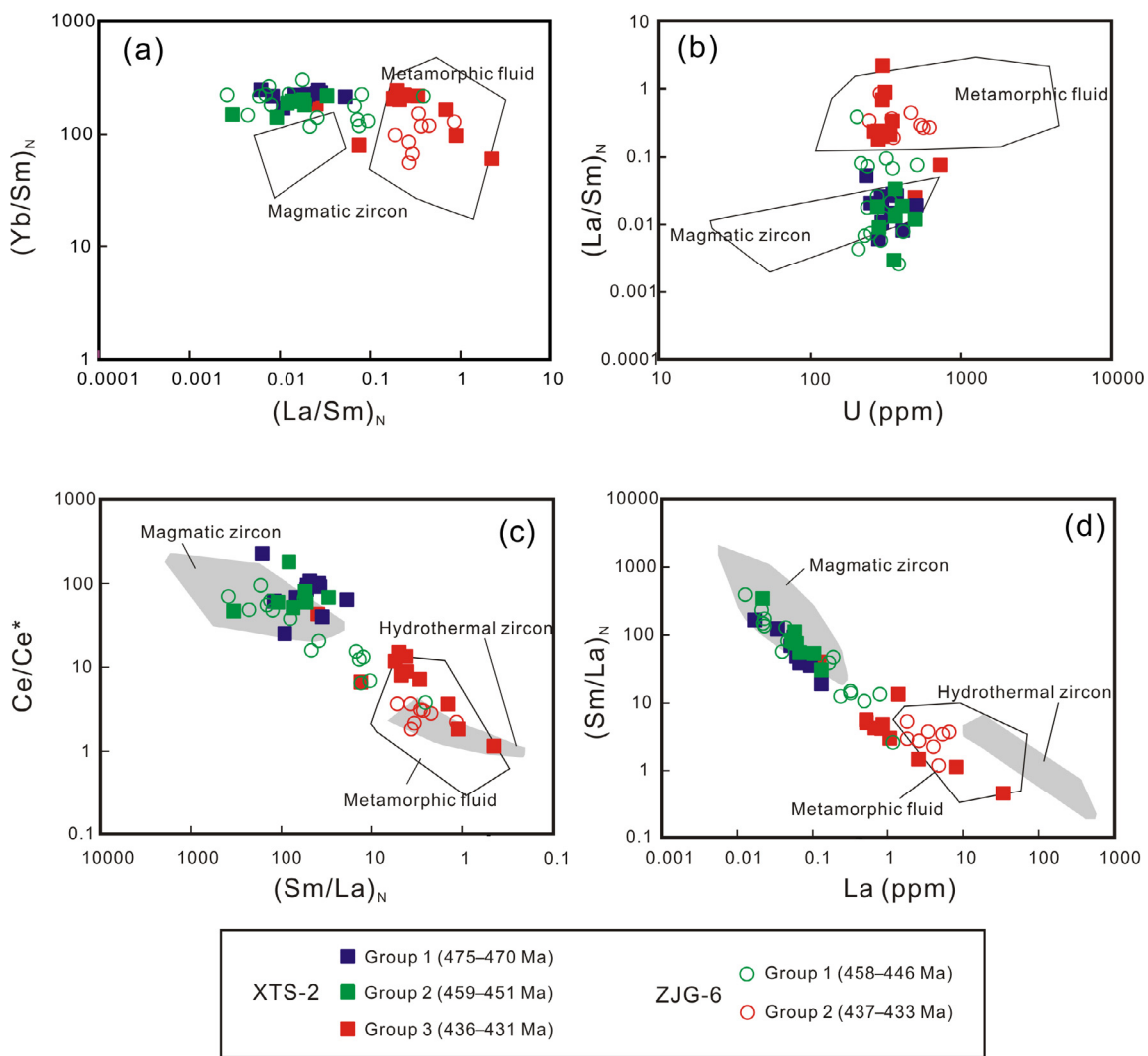


**Fig. 8.** Zircon type discriminations. (a)  $(\text{La}/\text{Sm})_N$  vs.  $(\text{Yb}/\text{Sm})_N$ ; (b) U vs.  $(\text{La}/\text{Sm})_N$ ; (c)  $(\text{Sm}/\text{La})_N$  vs.  $\text{Ce}/\text{Ce}^*$ . (d) La vs.  $(\text{Sm}/\text{La})_N$ . (a) and (b) after Xia et al. (2010); (c) and (d) after Hoskin (2005). "Metamorphic fluid" field in (c) and (d) after Xia et al. (2010).

### 6.3. Age of the footwall volcanism

Recent studies on long-lived arc volcanism have recognized a significant component of recycled, precursor materials present in late eruptions, as evidenced by disequilibrium assemblages, glomerocrysts (Nakamura, 1995; Watts et al., 1999; Tepley et al., 2000; Li et al., 2012, 2013b, 2016) and multiple crystal age populations (Schmitt, 2011; Cooper, 2015). As documented above, in this work, the youngest age population (440–430 Ma) represents the timing of massive metamorphic fluid activity during the orogeny. The group 2 zircons (460–451 Ma) from sample XTS-2 and group 1 zircons (458–447 Ma) from sample ZJG-6 have been concordantly constrained at  $456.7 \pm 4.4$  Ma (MSWD = 0.42) and  $453.1 \pm 3.4$  Ma (MSWD = 0.46), respectively, indicating that the older time limit on volcanism in the footwall of the Xitieshan deposit should be 450 Ma. This is also almost coincident with the cessation of ocean-continent subduction in the NMQB ( $\sim 460$  Ma; Xiong et al., 2014) and the peak metamorphic age of UHP eclogite from the Xitieshan area ( $\sim 450$  Ma; Chen et al., 2012). Thus, we infer 450 Ma as representing the age of footwall volcanism. The arc volcanism in the Xitieshan district may have started at ca. 500 Ma (Wang et al., 2000; Lu et al., 2002; Song et al., 2009; Chen et al., 2007) with two intense cycles of volcanism corresponding to the reported ages of 475–470 Ma and 460–450 Ma (Table 1).

### 6.4. Implications for exhalative ore-formation

In this study, the two critical time intervals for the latest volcanism (460–450 Ma) and subsequent massive metamorphic fluid activity (440–430 Ma) during the orogeny have been constrained. Thus, it follows that the timing of ore-formation and subseafloor exhalation should be limited to within the short time interval from 450 Ma to 440 Ma.

By comparing major VMS deposits all over the world, Allen et al. (2002) proposed that most exhalative mineralization at a given locality occurred within several million years, most within 1–2 million years. For most exhalative deposits in rifted-arc and back-arc settings (e.g., Li and Xi, 2012; Li et al., 2013a), the typical genetic model consists of three stages (Allen et al., 2002): 1) At X Ma, in an extensional tectonic setting, mantle upwelling and lithosphere thinning result in the formation of graben systems associated with the development of volcanic and sedimentary rocks, while arc volcanism gradually weakens; 2) At X + n Ma, triggered by the large-scale subseafloor fluid convection system usually associated with high-level felsic subvolcanic intrusions, strong sedimentary exhalation occurs at numerous chimneys controlled by structural conduits (such as the intersection of differently oriented faults, growth faults and calderas); 3) At X + n + X Ma, due to inversion of the tectonic setting from extension to compression, the subseafloor fluid convection system declines, while andesitic arc volcanism gradually increases again, followed by deformation, metamorphism and superimposed mineralization resulting from massive fluid activity within the earlier sedimentary rocks/ores.

Accordingly, we propose that the Xitieshan Pb-Zn deposit provides an excellent example of ore-forming processes associated with volcanism in rifted-arc/back-arc settings with the following genesis: 1) 500–450 Ma: the Xitieshan area was under a compressional tectonic setting, and volcanic and sedimentary rocks typical of a continental margin arc formed (Sun et al., 2012; Xiong et al., 2014); 2) 450–440 Ma: the tectonic setting changed from compression to extension, forming an intra-arc or back-arc (unclear at present) graben system. Supported by massive felsic subvolcanic intrusions in the upper levels of the graben system, a  $\sim 5$  km-long (equivalent to the length of the mining area) seafloor fluid convection system developed, resulting in sedimentary exhalative deposition on the seafloor, forming the precursors of the

conformable orebodies hosted in schist; 3) 440–430 Ma: the tectonic settings returned to compression again, triggered by the convergency between Qaidam and Oulongbuluke terranes in the late Early Paleozoic. During this time, metamorphic fluid dominated the region, resulting in zircon U-Pb isotopic resetting through recrystallization which yielded a younger age population. Subsequently, the subseafloor convection system was gradually extinguished, while intermediate-basic volcanism reappeared to overlap the early sedimentary sequences.

## 7. Conclusions

- (1) The metamorphism and related fluid alteration in the Tanjianshan Group occurred under a high-temperature (550–650 °C) condition, which overlaps with the lower temperature range of zircon crystallization (dominantly 600–750 °C) calculated by Ti-in-zircon thermometry. This may indicate that the metamorphism led to the modification of the original magmatic zircons, resulting in a younger age population of zircons.
- (2) Two cycles of volcanism (475–470 Ma and 460–450 Ma) have been differentiated for the footwall volcanic rocks in the Xitieshan Pb-Zn deposit. The subsequent exhalative Pb-Zn mineralization may have occurred over a short time interval of several million years (450–440 Ma). Intermediate-acidic magma-derived zircons were intensely affected by massive fluid activity during orogenic metamorphism and deformation which occurred from 440 to 430 Ma.

## Acknowledgements

This study was jointly supported by grants from National Natural Science Foundation of China (Grant Nos. 41172087, 41502067 and 41672074) and West Mining Corporation. Z.X. Feng, G.B. Wu, and Y.Q. Wang are acknowledged for their help in field investigation, sampling and exploration material collecting. Thanks are also due to Steven D. Scott and Jianwei Li for their help in polishing an earlier version of the manuscript. The authors wish to express their sincere appreciation to Ibrahim Uysal (Associate Editor), Axel K. Schmitt (Heidelberg University) and another anonymous reviewer for their detailed and insightful comments that greatly improved the manuscript.

## References

- Allen, R.L., Weihed, P., Blundell, D.J., 2002. Global comparisons of volcanic-associated massive sulphide districts. *Geol. Soc. Lond. Spec. Publ.* 204, 13–37.
- Andersen, T., 2002. Correction of common lead in U-Pb analyses that do not report  $^{204}\text{Pb}$ . *Chem. Geol.* 192, 59–79.
- Barrie, C.T., Amelin, Y., Pascual, E., 2002. U-Pb geochronology of VMS mineralization in the Iberian Pyrite Belt. *Miner. Deposita* 37, 684–703.
- Barth, A.P., Wooden, J.L., Jacobson, C.E., Economos, R.C., 2013. Detrital zircon as a proxy for tracking the magmatic arc system: The California arc example. *Geology* 41, 223–226.
- Bose, S., Sengupta, S., 2003. High temperature mylonitization of quartzofeldspathic gneisses: example from the Schirmacher Hills, East Antarctica. *Gondwana Res.* 6, 805–816.
- Carley, T.L., Miller, C.F., Wooden, J.L., Padilla, A.J., Schmitt, A.K., Economos, R.C., Bindeman, I.N., Jordan, B.T., 2014. Iceland is not a magmatic analog for the Hadean: Evidence from the zircon record. *Earth Planet. Sci. Lett.* 405, 85–97.
- Chalokwu, C.I., 1989. Epidote-amphibolite to amphibolites facies transition in the southern Appalachian Piedmont: *P-T* conditions across the garnet and calc-silicate isograds. *Geology* 17, 491–494.
- Chen, N.S., Wang, Q.Y., Chen, Q., Li, X.Y., 2007. Components and metamorphism of the basements of the Qaidam and Oulongbuluke micro-continental blocks, and a tentative interpretation of paleocontinental evolution in NW-Central China. *Earth Sci. Front.* 14, 43–55.
- Chen, L., Liu, Y., Hu, Z., Gao, S., Zong, K.Q., Chen, H.H., 2011. Accurate determinations of fifty-four major and trace elements in carbonate by LA-ICP-MS using normalization strategy of bulk components as 100%. *Chem. Geol.* 284, 283–295.

- Chen, D.L., Liu, L., Sun, Y., Sun, W.D., Zhu, X.H., Liu, X.M., Guo, C.L., 2012. Felsic veins within UHP eclogite at Xitieshan in North Qaidam, NW China: Partial melting during exhumation. *Lithos* 136–139, 187–200.
- Cooper, K.M., 2015. Timescales of crustal magma reservoir processes: insights from U-series crystal ages. *Geol. Soc. Lond. Spec. Publ.* 422 (1), 141–174.
- Deng, W.D., Kong, H., Xi, X.S., 2003. Geochemistry of the hydrothermal sedimentary Xitieshan Pb-Zn deposit, Qinghai Province (in Chinese with English abstract). *Bull. Mineral. Petrol. Geochim.* 22, 310–313.
- Feng, Z., Sun, H., Wu, G., Wang, Y., 2010. A discussion on type of the Xitieshan Pb-Zn ore deposit, Qinghai. *Geol. Rev.* 54, 501–512 (in Chinese with English abstract).
- Ferry, J.M., Waston, E.B., 2007. New thermodynamic models and revised calibrations for the Ti-in-zircon and Zr-in-rutile thermometers. *Contrib. Miner. Petrol.* 154, 429–437.
- Fu, J.G., 2015. Formation Age and Tectonic Attribute of the Tanjianshan Group in the Xitieshan Area, North Qaidam (Ph.D thesis). Graduate University of Chinese Academy of Sciences, pp. 1–156 (in Chinese with English abstract).
- Fu, J.G., Liang, X.Q., Wang, C., Zhou, Y., Jiang, Y., Dong, C.G., 2017. The Xitieshan volcanic sediment-hosted massive sulfide deposit, North Qaidam, China: Geology, structural deformation and geochronology. *Ore Geol. Rev.* 80, 923–946.
- Gao, X.Y., Zheng, Y.F., Chen, Y.X., Tang, H.L., Li, W.C., 2015. Zircon geochemistry records the action of metamorphic fluid on the formation of ultrahigh-pressure jadeite quartzite in the Dabie orogeny. *Chem. Geol.* 419, 158–175.
- Geisler, T., Rashwan, A.A., Rahn, M.K.W., Poller, U., Zwingmann, H., Pidgeon, R.T., Schleicher, H., Tomaschek, F., 2003. Low-temperature hydrothermal alteration of natural metamict zircons from the Eastern Desert, Egypt. *Mineral. Mag.* 67, 485–508.
- Hao, G.J., Lu, S.N., Wang, H.C., Xin, H.T., Li, H.K., 2004a. The Pre-Devonian tectonic framework in the northern margin of Qaidam basin and geological evolution of Olongbuluck paleo-block (in Chinese with English abstract). *Earth Science Frontiers* (China University of Geosciences, Beijing) 11: 115–122.
- Hao, G.J., Lu, S.N., Xin, H.T., Wang, H.C., 2004b. The constitution and importance geological events of Pre-Devonian in the Dulan, Qinghai (in Chinese with English abstract). *J. Jilin Univ.* 34, 495–501.
- Hoskin, P.W.O., 2000. Patterns of chaos: Fractal statistics and the oscillatory chemistry of zircon. *Geochim. Cosmochim. Acta* 64, 1905–1923.
- Hoskin, P.W.O., 2005. Trace-element composition of hydrothermal zircon and the alteration of Hadean zircon from the Jack Hills, Australia. *Geochim. Cosmochim. Acta* 69, 637–648.
- Hoskin, P.W.O., Black, L.P., 2000. Metamorphic zircon formation by solid-state recrystallization of protolith igneous zircon. *J. Metamorph. Geol.* 18, 423–439.
- Hou, Z., Deng, J., Sun, H., Song, S., 1999. Volcanogenic massive sulfide deposits in China: setting, feature, and style. *Explor. Min. Geol.* 8, 149–175.
- Hu, Z.C., Gao, S., Liu, Y.S., Hu, S.H., Chen, H.H., Yuan, H.L., 2008. Signal enhancement in laser ablation ICP-MS by addition of nitrogen in the central channel gas. *J. Anal. At. Spectrom.* 23, 1093–1101.
- Jackson, S.E., Pearson, N.J., Griffin, W.L., Belousova, E.A., 2004. The application of laser ablation-inductively coupled plasma-mass spectrometry to in-situ U-Pb zircon geochronology. *Chem. Geol.* 211, 47–69.
- Li, H., Xi, X.S., 2012. Geochemistry and sedimentary exhalative mineralization in Hutouya-Kendekeke field, Qinghai Province, China. *Chin. J. Nonferrous Met.* 22, 772–783 (in Chinese with English abstract).
- Li, H., Xi, X.S., 2015. Sedimentary fans: A new genetic model for sedimentary exhalative ore deposits. *Ore Geol. Rev.* 65, 375–389.
- Li, H.K., Lu, S.N., Wang, H.C., Xiang, Z.Q., Zheng, J.K., 2003. Quanji Group—the geological record of the Rodinia supercontinent break-up in the early Neoproterozoic preserved in the northern Qaidam margin, Qinghai, northwest China (in Chinese with English abstract). *Geol. Surv. Res.* 26, 27–37.
- Li, F., Wu, Z.L., Li, B.Z., Wang, L.F., 2006. Revision of the Tanjianshan Group on the northern margin of the Qaidam basin (in Chinese with English abstract). *Northwestern Geol.* 39, 83–90.
- Li, X.Y., Chen, N.S., Xia, X.P., Sun, M., Xu, P., 2007. Constraints on timing of the early Paleoproterozoic magmatism and crustal evolution of the Oulongbuluke microcontinent: U-Pb and Lu-Hf isotope systematic of zircons from Mohe granitic pluton (in Chinese with English abstract). *Acta Petrol. Sin.* 23, 513–522.
- Li, H., Xi, X.S., Wu, C.M., Zhang, D.B., 2012. Geochemistry and genesis of andesite from Zhaokalong Fe-Cu polymetallic deposit, Yushu, Qinghai. *J. Cent. South Univ.* 43, 3524–3534 (in Chinese with English abstract).
- Li, H., Xi, X.S., Wu, C.M., Watanabe, K., 2013a. Genesis of the Zhaokalong Fe-Cu polymetallic deposit at Yushu, China: Evidence from ore geochemistry and fluid inclusions. *Acta Geol. Sin.* 87, 486–500.
- Li, H., Watanabe, K., Xi, X.S., Yonezu, K., 2013b. Geochemistry of volcanic rocks at Zhaokalong iron-copper-polymetallic ore deposit, Qinghai Province, China: Implications for the tectonic background. *Procedia Earth Planet. Sci.* 6, 58–63.
- Li, H., Watanabe, K., Yonezu, K., 2014. Zircon morphology, geochronology and trace element geochemistry of the granites from the Huangshaping polymetallic deposit, South China: Implications for the magmatic evolution and mineralization processes. *Ore Geol. Rev.* 60, 14–35.
- Li, H., Xi, X.S., Sun, H.S., Kong, H., Wu, Q.H., Wu, C.M., Gabo-Ratio, J.A.S., 2016. Geochemistry of the Batang Group in the Zhaokalong area, Yushu, Qinghai: Implications for the Late Triassic tectonism in the northern Sanjiang region, China. *Acta Geol. Sin.* 90, 704–721.
- Li, H., Sun, H.S., Wu, J.H., Evans, N.J., Xi, X.S., Peng, N.L., Cao, J.Y., Gabo-Ratio, J.A.S., 2017. Re-Os and U-Pb geochronology of the Shazigou Mo polymetallic ore field, Inner Mongolia: Implications for Permian-Triassic mineralization at the northern margin of the North China Craton. *Ore Geol. Rev.* 83, 287–299.
- Liang, X.Q., Fu, J.G., Wang, C., Jiang, Y., Zhou, Y., Yang, Y.Q., Wang, Z.L., Pan, C.C., 2014. Redefinition and formation age of the Tanjianshan Group in Xitieshan region, Qinghai. *Acta Geol. Sin.* 88, 394–409.
- Liu, Y.S., Hu, Z.C., Gao, S., Günther, D., Xu, J., Gao, C.G., Chen, H.H., 2008. In situ analysis of major and trace elements of anhydrous minerals by LA-ICP-MS without applying an internal standard. *Chem. Geol.* 257, 34–43.
- Liu, Y.S., Gao, S., Hu, Z.C., Gao, C.G., Zong, K.Q., Wang, D.B., 2010a. Continental and oceanic crust recycling-induced melt-peridotite interactions in the Trans-North China Orogen: U-Pb dating, Hf isotopes and trace elements in zircons from mantle xenoliths. *J. Petrol.* 51, 537–571.
- Liu, Y.S., Hu, Z.C., Zong, K.Q., Gao, S., Xu, J., Chen, H.H., 2010b. Reappraisal and refinement of zircon U-Pb isotope and trace element analyses by LA-ICP-MS. *Chin. Sci. Bull.* 55, 1535–1546.
- Liu, X.C., Wu, Y.B., Gao, S., Wang, H., Zheng, J.P., Hu, Z.C., Zhou, L., Yang, S.H., 2014. Record of multiple stage channelized fluid and melt activities in deeply subducted slab from zircon U-Pb age and Hf-O isotope compositions. *Geochim. Cosmochim. Acta* 144, 1–24.
- Lu, S.N., Wang, H.C., Li, H.K., Yuan, G.B., Xin, H.T., Zheng, J.K., 2002. Redefinition of the Dakendaban Group on the northern margin of the Qaidam basin (in Chinese with English abstract). *Geol. Bull. China* 21, 19–23.
- Ludwig, K.R., 2003. Isoplot 3.00: A Geochronological Toolkit for Microsoft Excel. Berkeley Geochronology Center, Berkeley, CA.
- Mancktelow, N.S., Pennacchioni, G., 2004. The influence of grain boundary fluids on the microstructure of quartz-feldspar mylonites. *J. Struct. Geol.* 26, 47–69.
- Mathieu, R., Zetterstrom, K., Cuney, M., GauthierLafaye, F., Hidaka, H., 2001. Alteration of monazite and zircon and lead migration as geochemical tracers of fluid paleocirculations around the Oklo-Oke'lobondo and Bangombe natural nuclear reaction zones (Franceville basin, Gabon). *Chem. Geol.* 171, 147–171.
- Nakamura, M., 1995. Continuous mixing of crystal mush and replenished magma in the ongoing Unzen eruption. *Geology* 23, 807–910.
- Page, R., Laing, W., 1992. Felsic metavolcanic rocks related to the Broken Hill Pb-Zn-Ag orebody, Australia: Geology, depositional age, and timing of high-grade metamorphism. *Ecol. Geol.* 87, 2138–2168.
- Piercey, S., Peter, J., Mortensen, J., Paradis, S., Murphy, D., Tucker, T., 2008. Petrology and U-Pb geochronology of footwall porphyritic rhyolites from the Wolverine volcanogenic massive sulfide deposit, Yukon, Canada: Implications for the genesis of massive sulfide deposits in continental margin environments. *Ecol. Geol.* 103, 5–33.
- Rosa, D., Finch, A., Andersen, T., Inverno, C., 2009. U-Pb geochronology and Hf isotope ratios of magmatic zircons from the Iberian Pyrite Belt. *Miner. Petrol.* 95, 47–69.
- Schaltegger, U., Fanning, C.M., Gunther, D., Maurin, J.C., Schulmann, K., Gebauer, D., 1999. Growth, annealing and recrystallization of zircon and preservation of monazite in high-grade metamorphism: conventional and in-situ U-Pb isotope, cathodoluminescence and microchemical evidence. *Contrib. Miner. Petrol.* 134, 186–201.
- Schmitt, A.K., 2011. Uranium series accessory crystal dating of magmatic processes. *Annu. Rev. Earth Planet. Sci.* 39, 321–349.
- Schmitt, A.K., Vazquez, J.A., 2006. Alteration and remelting of nascent oceanic crust during continental rupture: Evidence from zircon geochemistry of rhyolites and xenoliths from the Salton Trough, California. *Earth Planet. Sci. Lett.* 252, 260–274.
- Shi, R.D., Yang, J.S., Wu, C.L., Iizuka, T., Hirata, T., 2006. Island arc volcanic rocks in the north Qaidam UHP belt, northern Tibet plateau: evidence for ocean-continent subduction preceding continent-continent subduction. *J. Asian Earth Sci.* 28, 151–159.
- Soman, A., Geisler, T., Tomaschek, F., Grange, M., Berndt, J., 2010. Alteration of crystalline zircon solid solutions: a case study on zircon from an alkaline pegmatite from Zomba-Malosa, Malawi. *Contrib. Miner. Petrol.* 160, 909–930.
- Song, S.G., Zhang, L.F., Niu, Y.L., 2004. Ultra-deep origin of garnet peridotite from the North Qaidam ultrahigh-pressure belt, Northern Tibetan Plateau, NW China. *Am. Mineral.* 89, 1330–1336.
- Song, S.G., Niu, Y.L., Zhang, L.F., Zhang, G.B., 2009. Time constraints on orogenesis from oceanic subduction to continental subduction, collision, and exhumation: An example from North Qilian and North Qaidam HP-UHP belts (in Chinese with English abstract). *Acta Petrol. Sin.* 25, 2067–2077.
- Sun, H.S., Zhao, L.J., Wu, G.B., Ning, J.T., Chen, Q.M., Jiang, C.L., 2012. Metallogenetic tectonic setting and ore-finding potential of Xitieshan massive sulfide lead-zinc deposit: Evidence from lithochemistry and geochemistry of ore-hosted volcanic strata, Tanjianshan Group. *Acta Petrol. Sin.* 28, 652–664 (in Chinese with English abstract).
- Tepley III, F.J., Davidson, J.P., Tilling, R.I., Arth, J.G., 2000. Magma mixing, recharge, and eruption histories recorded in plagioclase phenocrysts from El Chicho'n Volcano, Mexico. *J. Petrol.* 41, 1397–1411.
- Troitzsch, U., Christy, A.G., Ellis, D.J., 2004. Synthesis of ordered zirconium titanate ( $Zr, Ti_2O_4$ ) from the oxides using fluxes. *J. Am. Ceram. Soc.* 87, 2058–2063.
- Wang, X., Kienast, J.R., 1999. Morphology and geochemistry of zircon: a case study on zircon from the microgranitoid enclaves. *Sci. China* 42, 544–552.
- Wang, J.C., Peng, E.S., Sun, Z.J., 2000. Tectonic reconstruction of the Xitieshan Pb-Zn deposit after spout sedimentation, Qinghai Province. *Geotectonica et Metallogenesis* 84, 163–169.
- Wang, H.C., Lu, S.N., Yuan, G.B., Xin, H.T., Zhang, B.H., Wang, Q.H., Tian, Q., 2004. Tectonic setting and age of the Tanjianshan Group on the northern margin of the Qaidam basin (in Chinese with English abstract). *Geol. Bull. China* 22, 487–493.

- Wang, X., Griffin, L.W., Jie, C., Huang, P.Y., Li, X., 2011. U and Th contents and Th/U ratios of zircon in felsic and mafic magmatic rocks: Improved zircon-melt distribution coefficients. *Acta Geol. Sin.* 85, 164–174.
- Watson, E.B., Harrison, T.M., 2005. Zircon thermometer reveals minimum melting conditions on earliest Earth. *Science* 308, 841–844.
- Watson, E.B., Wark, D.A., Thomas, J.B., 2006. Crystallization thermometers for zircon and rutile. *Contrib. Miner. Petrol.* 151, 413–433.
- Watts, R.B., de Silva, S.L., Jimenez de, R.G., Croudace, I., 1999. Effusive eruption of viscous silicic magma triggered and driven by recharge: a case study of the Cerro Chason-Runtu Jarita Dome complex in southwest Bolivia. *Bull. Volcanol.* 60, 241–264.
- Wiedenbeck, M., Alle, P., Corfu, F., Griffin, W.L., Meier, M., Oberli, F., Quadat, A.V., Roddick, J.C., Spiegel, W., 1995. Three natural zircon standards for U-Th-Pb, Lu-Hf, trace element and REE analyses. *Geostand. Geoanal. Res.* 19, 1–23.
- Wu, J.R., Ren, B.C., Zhang, M., Gao, D.C., 1987. Classification and characteristics of the Xitieshan massive sulfide deposit in Qinghai Province, China (in Chinese). Institute Periodical, Xi'an Geology and Mineral Resources Research Institute, Chin. Acad. Geol. Sci. 20, 1–30.
- Wu, C.L., Yang, J.S., Xu, Z.Q., Wooden, J.L., Ireland, T., Li, H.B., Shi, R.D., Meng, F.C., Chen, Y.S., Persing, H., Meibom, A., 2004. Granitic magmatism on the early Paleozoic UHP belt of northern Qaidam, NW China (in Chinese with English abstract). *Acta Geol. Sin.* 78, 658–664.
- Wu, C.L., Gao, Y.H., Wu, S.P., Chen, Q.L., Wooden, J.L., Mazadab, F.K., Mattinson, C., 2007. Zircon SHRIMP U-Pb dating of granites from the Da Qaidam area in the north margin of Qaidam basin, NW China (in Chinese with English abstract). *Acta Petrolog. Sin.* 23, 1861–1875.
- Xia, Q.X., Zheng, Y.F., Hu, Z.C., 2010. Trace elements in zircon and coexisting minerals from low-T/UHP metagranite in the Dabie orogen: implications for action of supercritical fluid during continental subduction-zone metamorphism. *Lithos* 114, 385–412.
- Xin, H.T., Wang, H.C., Zhou, S.J., 2006. Geological events and tectonic evolution of the north margin of the Qaidam basin. *Geol. Surv. Res.* 29, 311–320 (in Chinese with English abstract).
- Xiong, X.W., Chen, Y.Y., 1994. Early Paleozoic taphrogenic trough in the north margin of Qaidam terrane. In: Wang, H.Z., Wang, Z.Q., and Zhang, L.H., (eds), *Meso-Neo-proterozoic and Paleozoic tectonic evolution in the ancient continental margin of China* (in Chinese). Conference Proceedings, Geological Publishing House 1, 114–131.
- Xiong, Q., Zheng, J.P., Griffin, W.L., O'Reilly, S.Y., Pearson, N.L., 2014. Pyroxenite dykes in orogenic peridotite from North Qaidam (NE Tibet, China) track metasomatism and segregation in the mantle wedge. *J. Petrol.* 55, 2347–2376.
- Xu, Z.Q., Yang, J.S., Wu, C.L., Li, H.B., Zhang, J.X., Qie, X.X., Song, S.G., Wan, Y.S., Chen, W., Qiu, H.J., 2003. Timing and mechanism of formation and exhumation of the Qaidam ultra-pressure metamorphic belt. *Acta Geol. Sin.* 77, 163–176 (in Chinese with English abstract).
- Yang, J.S., Song, S.G., Xu, Z.Q., Wu, C.L., Shi, R.D., Zhang, J.X., Li, H.B., Wan, Y.S., Liu, Y., Qiu, H.J., Liu, F.L., Maruyama, S., 2001. Discovery of coesite in the north Qaidam Early Paleozoic ultrahigh-high pressure (UHP-HP) metamorphic belt, NW China. *Acta Geol. Sin.* 75, 175–179 (in Chinese with English abstract).
- Yuan, G.B., Wang, H.C., Li, H.M., Hao, G.J., Xin, H.T., 2002. Zircon U-Pb age of the gabbros in Luliangshan area on the northern margin of Qaidam basin and its geological implication. *Prog. Precambrian Res.* 25, 36–40 (in Chinese with English abstract).
- Zhang, D.Q., She, H.Q., Feng, C.Y., Li, D.X., Li, J.W., 2009a. Geology, age, and fluid inclusions of the Tanjianshan gold deposit, western China: Two orogenies and two gold mineralizing events. *Ore Geol. Rev.* 36, 250–263.
- Zhang, J.X., Mattinson, C.G., Meng, F.C., Yang, H.J., Wan, Y.S., 2009b. U-Pb geochronology of paragneisses and metabasite in the Xitieshan area, north Qaidam Mountains, western China: Constraints on the exhumation of HP/UHP metamorphic rocks. *J. Asian Earth Sci.* 35, 245–258.
- Zhang, G.B., Zhang, L.F., Christy, A., 2013. From oceanic subduction to continental collision: An overview of HP-UHP metamorphic rocks in the north Qaidam UHP belt, NW China. *J. Asian Earth Sci.* 63, 98–111.
- Zhao, F.Q., Guo, J.J., Li, H.K., 2003. Geological characteristics and isotopic age of Tanjianshan Group along northern margin of Qaidam basin. *Geol. Bull. China* 22, 28–31 (in Chinese with English abstract).
- Zhu, X.Y., Deng, J.N., Wang, J.B., Lin, L.J., Fan, J.C., Sun, S.Q., 2007. Identification and study of stockwork altered pipe of Xitieshan lead-zinc deposit, Qinghai Province. *Geochimica* 36, 37–48 (in Chinese with English abstract).